J Mater Sci

Metals & corrosion

High-entropy CoCrFeMnNi coatings produced by co-electrodeposition and subsequent heat treatment

Mateusz Włoczewski[1,2], Dariusz M. Jarząbek[2,3,*], and Dariusz Oleszak[1]

[1] *Faculty of Materials Science and Engineering, Warsaw University of Technology, Woloska Str. 141, 02-507 Warsaw, Poland*
[2] *Institute of Fundamental Technological Research, Polish Academy of Sciences, Pawińskiego 5B, 02-106 Warsaw, Poland*
[3] *Faculty of Mechatronics, Warsaw University of Technology, Boboli Str. 8, 02-525 Warsaw, Poland*

Received: 19 March 2026
Accepted: 4 June 2026

ABSTRACT

Developing thick and well-adhered high-entropy alloy (HEA) coatings remains a major technological challenge due to the high cost and complexity of existing deposition methods. This study introduces a novel hybrid approach that combines mechanical alloying, electrochemical co-deposition, and high-temperature annealing to fabricate CoCrFeMnNi-based coatings. In this process, HEA powders obtained by mechanical alloying are suspended in a classical Watts bath and co-electrodeposited with nickel onto copper and steel substrates. Subsequent annealing promoted homogenization and diffusion between the coating and substrate, producing coatings up to approximately 100 μm thick, although residual porosity remained an important issue requiring further optimization. Structural and chemical analyses revealed face-centered cubic solid solutions with good adhesion, as indicated by the absence of cracking and delamination during scratch testing, and a maximum hardness of 6.25 GPa. The use of co-electrodeposition enables easy incorporation of complex HEA compositions using conventional electrochemical equipment, drastically reducing the cost and process temperature compared with vapor- or laser-based methods. The developed technology not only overcomes the limitations of direct HEA electrodeposition but also allows the deposition of coatings on complex geometries using environmentally friendly aqueous electrolytes. This simple yet versatile approach opens new pathways for producing high-performance protective coatings for applications in energy, aerospace, and nuclear industries, where mechanical robustness and chemical stability at elevated temperatures are critical.

Handling Editor: Jae-il Jang.

Address correspondence to E-mail: djarz@ippt.pan.pl

https://doi.org/10.1007/s10853-026-13158-0

Introduction

High-entropy alloys (HEAs) represent a relatively new class of metallic materials, first introduced in 2004 [1]. Their concept is rooted in the idea of configurational (mixing) entropy, which favors the formation of stable, single-phase solid solutions rather than complex intermetallic compounds. Over the past two decades, two complementary definitions of HEAs have been established [1–4]:

(1) Composition-based definition: HEAs are alloys with five or more principal elements, each present in concentrations between 5 and 35 at%. Minor alloying additions up to 5 at% are also permissible.
(2) Entropy-based definition: HEAs are alloys characterized by a high configurational entropy, typically exceeding 1.61R (where *R* is the gas constant, 8.314 J/mol·K).

High-entropy alloys (HEAs) represent a highly promising class of advanced materials distinguished by a unique combination of properties rarely achievable in conventional alloys. They exhibit exceptional hardness, strength, and ductility, accompanied by remarkable resistance to heat, radiation, and corrosion [2, 5]. However, the fabrication of bulk HEAs remains costly, mainly due to the high content of expensive alloying elements. A practical strategy to overcome this limitation is to apply HEAs as protective coatings on inexpensive substrates, combining superior surface performance with economical material use. To achieve this, numerous deposition techniques have been investigated, including electrochemical deposition [6], cathodic arc deposition [7], laser cladding [8], magnetron sputtering [9, 10], and thermal spraying [11].

Unfortunately, the above methods all exhibit limitations, such as process complexity, high equipment costs, challenges in coating complex geometries, poor substrate adhesion, high defect densities, or high gas contents [12]. Among the available methods, electrochemical deposition is regarded as the most practical and versatile approach. This relatively simple and cost-effective method allows for the deposition of metal coatings on complex geometries, and the necessary equipment is already available in many manufacturing plants. Additionally, it has low raw material and energy requirements, low operating temperatures, relatively short synthesis times, uncomplicated equipment, and high scalability [13–15]. However, research on the electrodeposition of multicomponent HEAs (five or more components) is still preliminary, with few associated reports [16, 17]. It is challenging to achieve a uniform distribution and compositional control [18, 19] of multiple elements during electrodeposition because of the deposition kinetics and preferential deposition of certain elements, which can lead to a nonuniform elemental distribution and microstructure.

To overcome the drawbacks of conventional techniques, this work introduces a novel electrochemical-based route for producing HEA coatings. Specifically, a single metal matrix with HEA particles is formed by co-electrodeposition, followed by a homogenizing heat treatment (Fig. 1). In this study, the term co-electrodeposition is used to describe an electrochemical composite deposition process, in which metal ions (Ni) are reduced on the cathode surface while solid HEA powder particles suspended in the electrolyte are simultaneously incorporated into the growing metal layer. This approach enables the formation of a metal–particle composite coating in a single electrochemical step. First, mechanical alloying is used to produce the HEA powder. In the subsequent step, nickel and the HEA powder are co-electrodeposited onto the cathode substrate using an electrochemical bath. Two compositions of mechanically alloyed powders are applied in this study: CoCrFeMnNi (with Ni) and CoCrFeMn (without Ni). In the latter case, nickel is introduced solely through the chemical solution during the electrochemical deposition. The final step involves annealing the obtained composite coating to promote the dissolution of HEA particles within the matrix. As this study is the first to implement this specific combination of techniques, CoCrFeMnNi was selected as the model alloy owing to its well-documented properties and status as one of the most thoroughly investigated HEAs. In this study, a classical Watts bath [20] was used as an electrochemical solution. This choice, similar to that of the model alloy, was motivated by practical considerations—the Watts bath is a well-established and widely used system with thoroughly characterized properties and well-defined process parameters. One of its key advantages is that it is an aqueous solution, making it considerably less toxic than organic solvent-based electrolytes. Additional benefits include its wide availability and low cost. Finally, the microstructures of

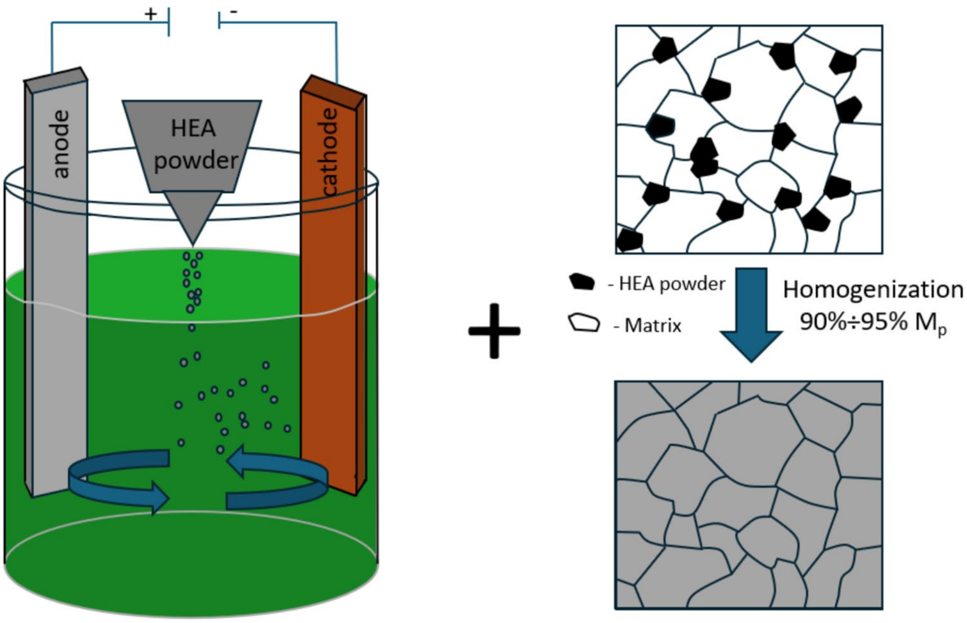

Figure 1 Schematic of HEA coating process with co-electrodeposition (left) followed by homogenizing heat treatment (right).

the obtained coatings were studied using scanning electron microscopy (SEM), energy dispersive X-ray spectroscopy (EDS), and X-ray diffraction (XRD), while their mechanical properties were evaluated via nanoindentation.

Experimental

Sample preparation

To verify the proposed method for preparing HEA coatings, two mechanically alloyed equimolar powders (CoCrFeMnNi and CoCrFeMn) and two substrates (copper and steel) were used. The hybrid method combines three processes: mechanical alloying, electrochemical co-deposition, and annealing.

First, CoCrFeMnNi and CoCrFeMn powders were prepared by mechanical alloying using a planetary ball mill (Fritsch P5). The ratio of steel balls to powder was 10:1, and the powder container was placed in a protective argon atmosphere. The total ball-milling time was 50 h, with a sequence of 15 min milling and 5 min braking. The resulting powders were collected for further processing.

Next, composite coatings were produced by electrochemical co-deposition. During this process (also referred to here as co-electrodeposition), nickel ions are reduced on the cathode surface while suspended HEA powder particles are simultaneously incorporated into the growing nickel layer. As a result, the obtained coating is a metal–particle composite rather than a purely metallic film. Nickel electroplating was carried out in a classical Watts bath [20] modified by the addition of sodium lauryl sulfate (SLS) and KCl to reduce the surface roughness of the deposited coating. The electrolyte composition is summarized in Table 1. HEA powders were then added to the prepared baths. Two types of electrolytes were formulated in this way: one containing CoCrFeMnNi powder and another containing CoCrFeMn powder The co-electrodeposition conditions were identical for both baths: solution temperature of 60 °C; plating time of 80 min; pH, approximately 4.0; and current density of 0.22 mA/mm^2. Throughout the process, the electrolyte was mechanically stirred to ensure uniform suspension of the HEA particles. According to previous studies [21] the main reactions during nickel

Table 1 Electrolyte composition

Component	$NiSO_4$	$NiCl_2$	H_3BO_3	SLS[a]	KCl	Saccharin
Concentration [g/l]	300	45	45	0.2	6	3

[a] SLS – sodium lauryl sulfate

electrodeposition from a Watts bath, examined using a voltammetric, involve the reduction of nickel ions, boric acid and hydrogen ions at the cathode, while oxygen evolution and chloride oxidation occur at the anode. In this work, a parallel-plate configuration with single-sided electrodes was used, employing a high-purity nickel anode and either copper or steel cathodes. Copper was chosen because its lattice constant is close to that of nickel, which helps minimize interfacial stress and prevents delamination. However, its relatively low melting point limits the annealing temperature during subsequent processing. Steel on the other hand, allows for higher annealing temperatures, promoting enhanced diffusion and homogenization of the coating. Consequently, four series of samples were prepared (the sample names are provided in brackets):

(A) Nickel matrix and CoCrFeMnNi particles deposited on copper substrate (Ni + CoCrFeMnNi on copper),
(B) Nickel matrix and CoCrFeMn particles deposited on copper substrate (Ni + CoCrFeMn on copper),
(C) Nickel matrix and CoCrFeMnNi particles deposited on steel substrate (Ni + CoCrFeMnNi on steel), and
(D) Nickel matrix and CoCrFeMn particles deposited on steel substrate (Ni + CoCrFeMn on steel).

The final stage of the process involved annealing for 12 h. The annealing temperature was set to approximately 90% of the melting point of the lowest-melting constituent—920 °C for samples on copper substrates and 1120 °C for those on steel. Following this treatment, four series of annealed coatings were obtained.

(A) Ni/CoCrFeMnNi on copper substrate,
(B) Ni/CoCrFeMn on copper substrate,
(C) Ni/CoCrFeMnNi on steel substrate and
(D) Ni/CoCrFeMn on steel.

For clarity, the nomenclature adopted in this study defines " + " as a composite coating before annealing (nickel matrix with incorporated HEA powder) and "/" as the homogenized coating after annealing. The experimental conditions are summarized in Table 2.

Table 2 Sample summary and experimental conditions

Sample number	Substrate	Powder added to electrolyte	Annealing temperature
1	Copper	CoCrFeMnNi	920 °C
2		CoCrFeMn	
3	Steel	CoCrFeMnNi	1120 °C
4		CoCrFeMn	

Microstructural characterization

The morphologies of the mechanically alloyed powders and HEA coatings were determined by SEM (Zeiss Crossbeam 350) and EDS. The EDS data were analyzed using EDAX TEAM. The powder particle size distribution was measured using a Kamika Instruments Mini 3D device with an ultrasound frequency of 40 Hz and amplitude of a few millimeters to separate the particles. The measurement involved measuring the particles in a parallel beam of light, and the output was the signal received by the photodiode. The phase compositions of the powders and coatings were determined by XRD (Rigaku MiniFlex) with Cu Kα radiation ($\lambda = 1.5418$ Å in the 2θ range of 20°–100°. The step size and interval were 0.05° and 5 s, respectively, and the measurement was conducted using standard Bragg–Brentano geometry.

Nanohardness measurements

The mechanical properties of the prepared coatings were evaluated by nanoindentation. The tests were carried out using an in situ SEM Alemnis nanoindenter equipped with a diamond Berkovich tip. Prior to the measurements, continuous stiffness measurement calibration was performed on a fused silica reference sample [22, 23]. Indentation tests were conducted at two maximum loads, 10 and 50 mN, with five measurements performed for each sample. Thermal drift and instrumental effects were corrected using the manufacturer's software, which was also employed to analyze the data. The hardness values were determined according to the Oliver–Pharr method [23].

Scratch-test

The adhesion of the coatings was evaluated by scratch testing using an in situ SEM Alemnis nanoindenter. The tests were carried out using a diamond spherical tip with a radius of 10 μm as a counter body, scratch length 25 μm and linearly increasing normal load from 0 up to 25 mN.

Results

Mechanical alloying

The phase compositions of the CoCrFeMnNi and CoCrFeMn powders after 50 h of mechanical alloying are shown in Fig. 2. Both materials exhibited dual-phase structures with body-centered cubic (BCC) and face-centered cubic (FCC) phases. Based on thermodynamic and atomic parameters – including mixing enthalpy, atomic size difference, mixing entropy, valence electron concentration, and the Ω criterion [2, 24, 25]—the CoCrFeMnNi alloy is theoretically expected to form a single FCC solid solution, as confirmed by previous empirical studies [26, 27]. Nevertheless, the formation of dual-phase CoCrFeMnNi alloys is common in mechanically alloyed systems and has been widely reported [28, 29]. This behaviour is attributed to the formation of metastable phases through solid-state reactions during high-energy milling process [30]. Mechanically alloyed HEA powders also retain a substantial amount of stored energy arising from internal stresses and high density of defects such as dislocations and grain boundaries [31]. This excess energy reduces the activation barrier for phase transformation and facilitates the evolution of a stable FCC phase during subsequent high-temperature processing, such as spark plasma sintering [28] or annealing, as applied in the present study.

The particle size distributions of both alloy powders are shown in Fig. 3. For both systems, the majority of particles ranged between 30 and 40 μm in diameter. However, the maximum particle sizes differed noticeably between the two alloys: the largest CoCrFeMnNi particles reached approximately 113 μm, whereas those of CoCrFeMn extended up to 178 μm. Although powders with particle sizes below 100 μm were initially used for mechanical alloying, larger agglomerates formed during milling as a result of particle adhesion and cold welding. The tendency of CoCrFeMn to form larger agglomerates can be attributed to its higher ductility and resistance to crushing during

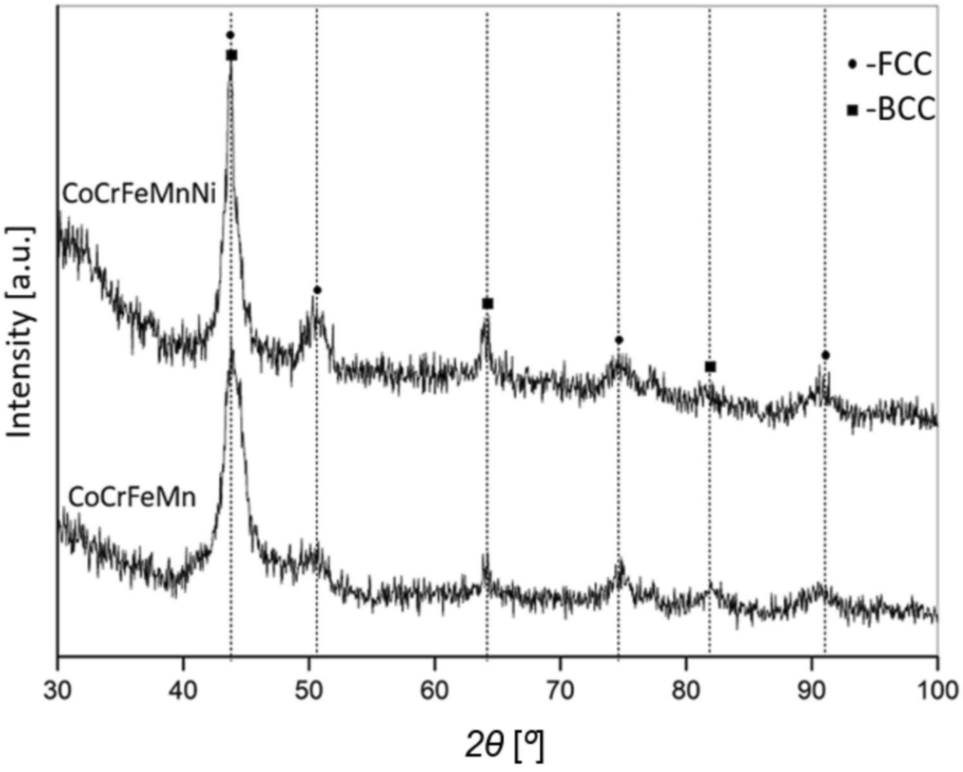

Figure 2 XRD patterns of CoCrFeMnNi and CoCrFeMn powders after mechanical alloying.

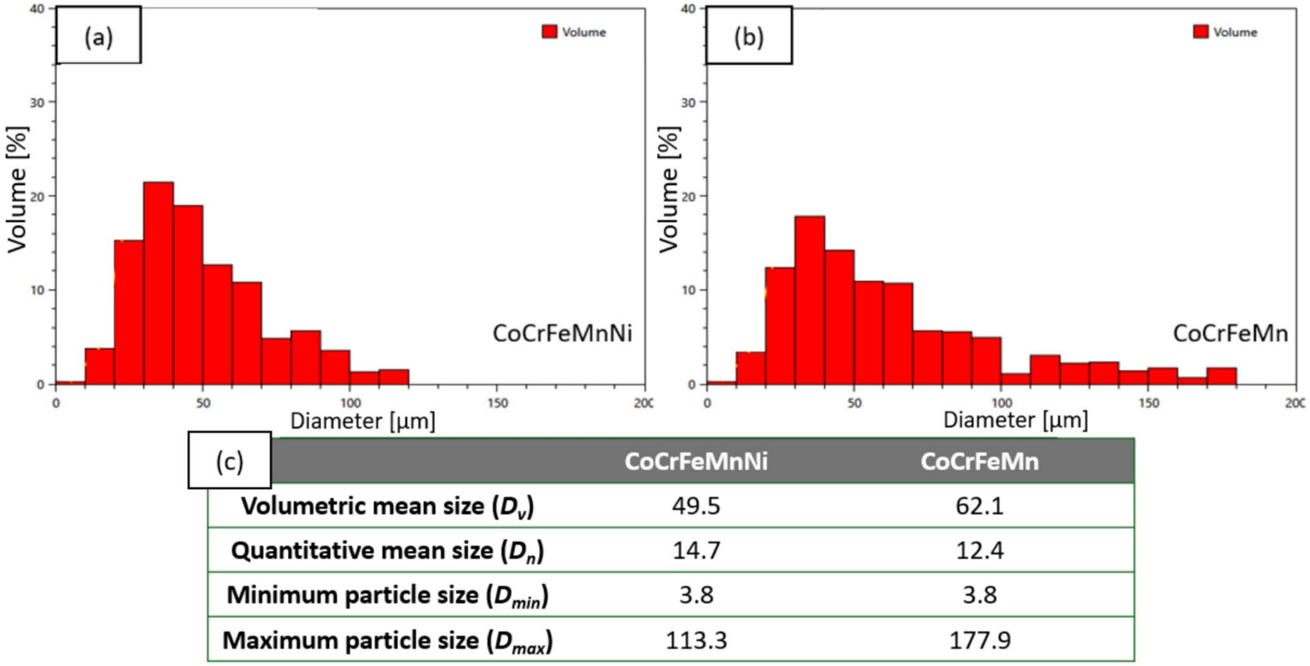

	CoCrFeMnNi	CoCrFeMn
Volumetric mean size (D_v)	49.5	62.1
Quantitative mean size (D_n)	14.7	12.4
Minimum particle size (D_{min})	3.8	3.8
Maximum particle size (D_{max})	113.3	177.9

Figure 3 Particle size distribution of mechanically alloyed powders: **a** CoCrFeMnNi and **b** CoCrFeMn.

milling. In contrast, the CoCrFeMnNi alloy, which exhibits stronger lattice distortion—a characteristic feature of high-entropy alloys intensified by the presence of multiple principal elements—tends to be more brittle. This increased brittleness limits particle growth and results in a smaller maximum particle size.

The morphologies of the mechanically alloyed CoCrFeMnNi and CoCrFeMn particles are shown in Fig. 4. The CoCrFeMnNi particles (Fig. 4a, b) exhibited a relatively uniform size distribution and a predominantly globular morphology, consistent with the particle size analysis. In contrast, the CoCrFeMn particles (Fig. 4c, d) displayed a broader size distribution and more irregular, angular shapes. These differences arise from the distinct mechanical behaviors of the alloys during milling—the higher ductility of CoCrFeMn promotes plastic deformation and cold welding, leading to irregular particle shapes, whereas the increased brittleness of CoCrFeMnNi, associated with its greater lattice distortion, favors particle fragmentation and rounding during the high-energy impacts of the milling process.

Elemental distributions within the mechanically alloyed powders were examined using EDS, and the corresponding elemental maps are shown in Fig. 5. Both alloys exhibited a generally uniform distribution of the principal elements, confirming effective mixing during the mechanical alloying process. Minor local variations, particularly regions with slightly elevated iron concentrations, were occasionally observed. These inhomogeneities most likely originated from abrasion of the steel milling tools during the mechanical alloying process. Overall, the EDS analysis confirms that extended high-energy milling resulted in near-homogeneous multi-element powders suitable for subsequent co-electrodeposition.

Electrochemical co-deposition

The next step involved the electrochemical co-deposition of the mechanically alloyed powders within a nickel matrix. Suspensions of the CoCrFeMnNi and CoCrFeMn powders were prepared in classical Watt baths, and electrochemical co-deposition was conducted on steel and copper substrates. Figure 6a compares the morphology of Ni + CoCrFeMnNi coating (right) with that of a pure nickel coating (left) under an optical microscope, revealing pronounced morphological differences. While the pure nickel coating conformed to the topography of the substrate, the co-electrodeposited Ni + CoCrFeMnNi coating was significantly rougher. Moreover, its morphology resembled that of the CoCrFeMnNi powder itself (Fig. 6b),

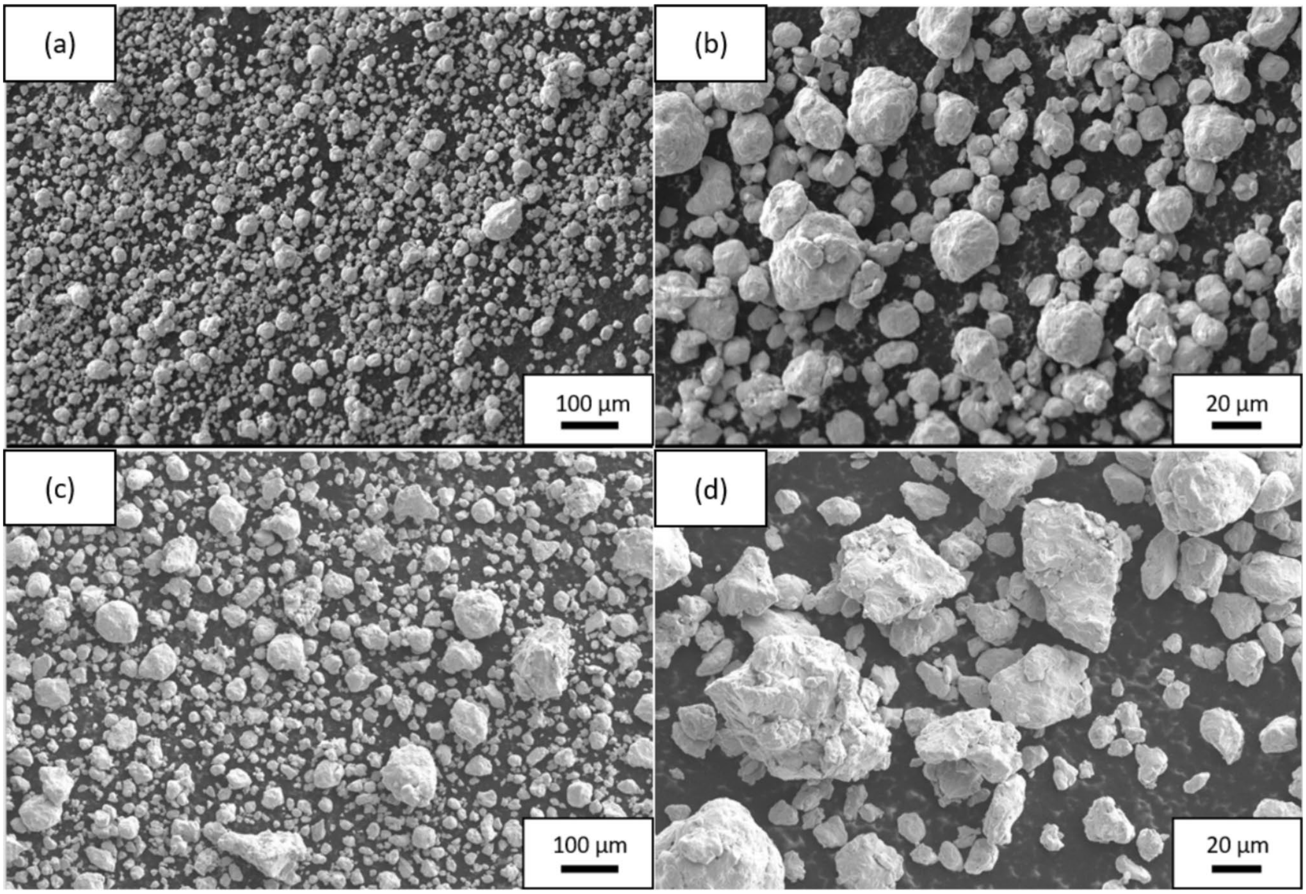

Figure 4 SEM images of mechanically alloyed powders: **a**, **b** CoCrFeMnNi and **c**, **d** CoCrFeMn.

indicating that the size and shape of the alloy particles had a strong influence on the surface texture of the resulting composite coating.

Figure 7 presents surface SEM images of the co-electrodeposited composite coatings obtained on both substrates. No significant morphological differences were observed between the samples. In both cases, the entire substrate surface was uniformly covered by a composite coating of nickel matrix embedding HEA powder particles. During co-electrodeposition process, the powder particles are transported toward the cathode along with a cloud of nickel ions, which are subsequently reduced on the cathode surface. The reduced nickel and entrapped powder particles adhere to the substrate, forming a composite coating, consistent with the mechanism previously proposed in the literature [32].

Preparing cross-sections of the co-electrodeposited samples proved challenging, as the hard HEA particles tended to detach or tear during cutting. Considering the limited penetration depth in EDS analysis, signals from the cross-sectional measurements would predominantly originate from the nickel matrix; therefore, EDS was performed on the coating surface instead. Figure 8a,b show the surface SEM image and the corresponding EDS elemental map of the Ni + CoCrFeMnNi coating on copper, while Fig. 8c presents EDS spectra collected from three distinct regions. Here, nickel stems from both the HEA particles and the matrix. The EDS map, color-coded in red, blue, and yellow, illustrates the spatial variation in elemental composition, with the corresponding spectra displayed on the right-hand side of the figure. The peak intensities of Co, Cr, Fe, and Mn (indicative of the HEA powder) were the lowest in the red areas and highest in the yellow regions, suggesting that the latter correspond to particles with thinnest nickel layers. The EDS spectra thus confirmed the incorporation of HEA particles within a nickel matrix, although the concentrations of Co, Cr, Fe, and Mn were below equimolar levels.

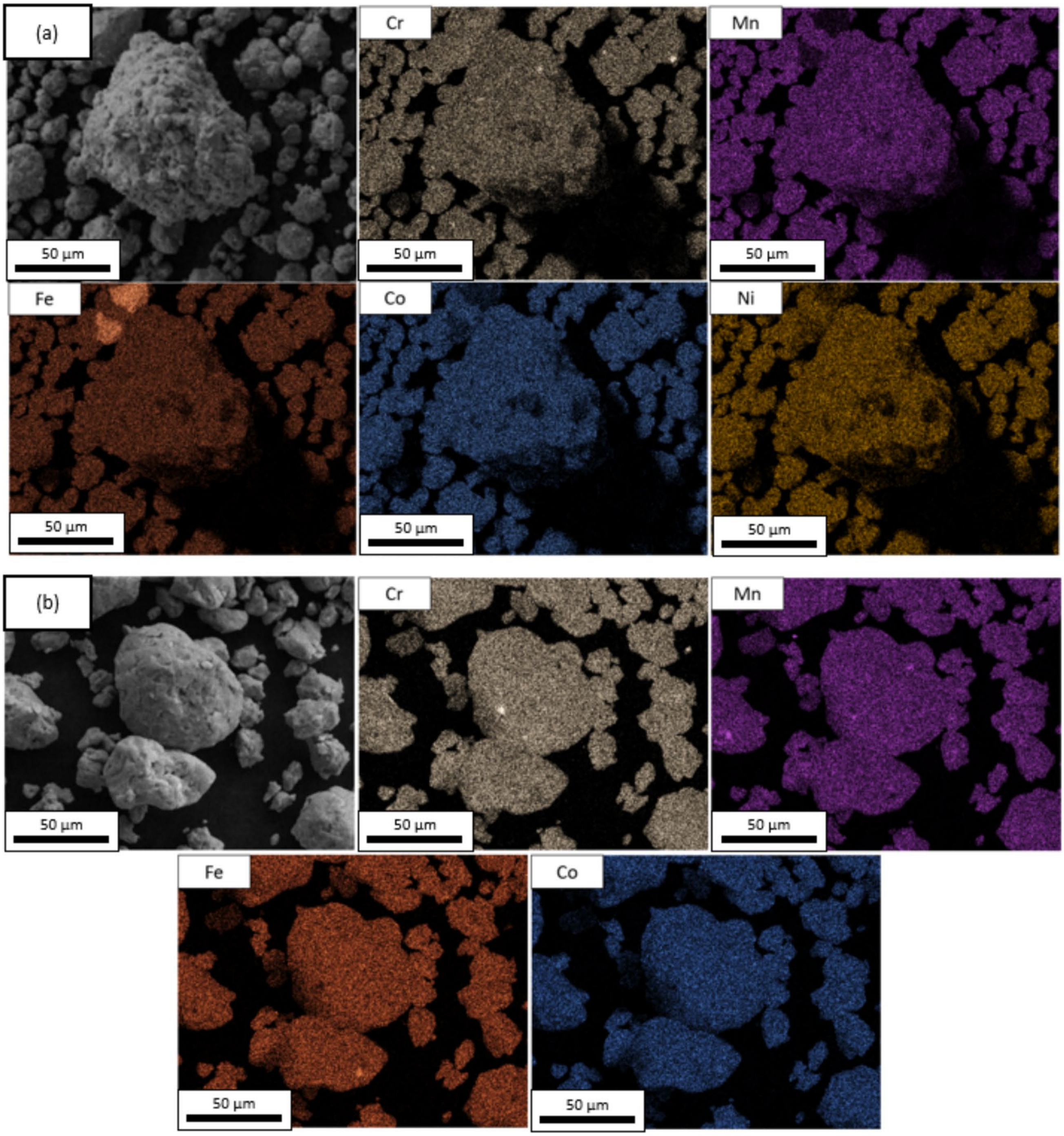

Figure 5 EDS elemental maps of mechanically alloyed powders: **a** CoCrFeMnNi and **b** CoCrFeMn.

To complement the EDS analysis and overcome its inherent limitations, X-ray diffraction (XRD) measurements were performed on the coatings prior to annealing to verify the presence of HEA powder particles. Figure 9 shows XRD pattern of the co-deposited Ni + CoCrFeMnNi coating on a copper substrate. The diffraction peaks correspond to an FCC phase attributed to nickel, as well as additional BCC and FCC reflections originating from the incorporated HEA particles. The coexistence of these phases confirms the successful co-deposition process of the HEA powder within the nickel matrix.

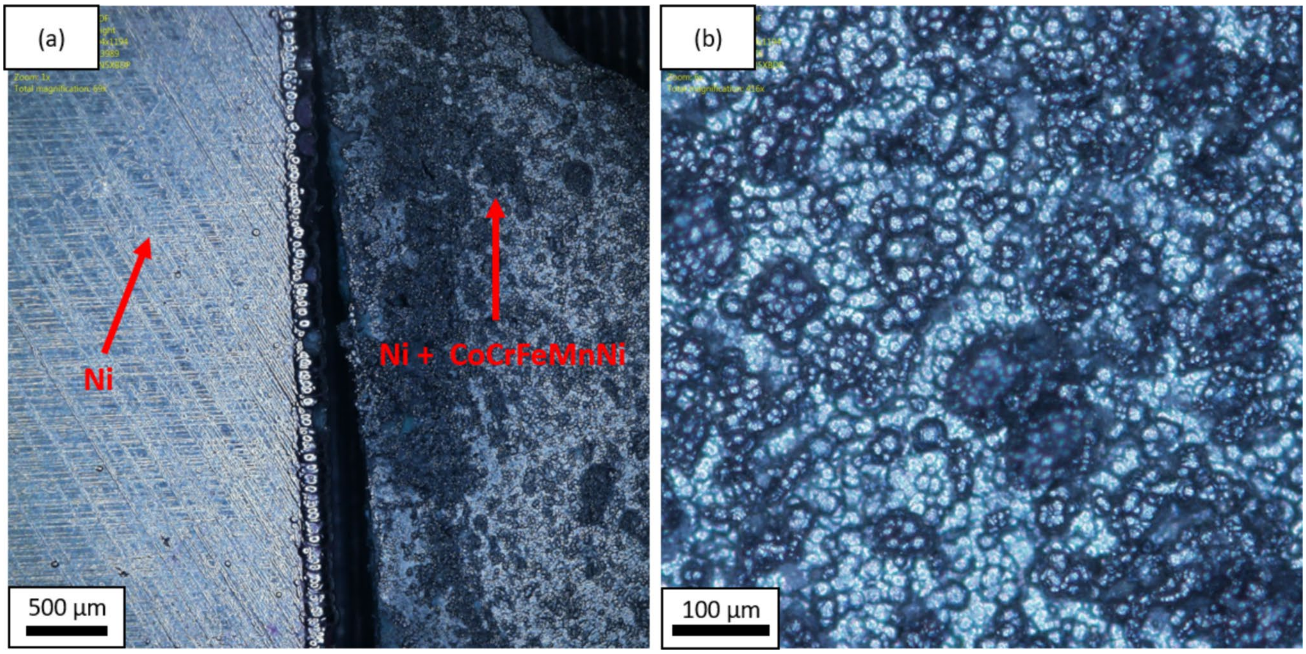

Figure 6 Dark-field optical micrographs of **a** electrochemically deposited nickel (left) and co-deposited Ni + CoCrFeMnNi (right) and **b** the surface of the Ni + CoCrFeMnNi coating at higher magnification.

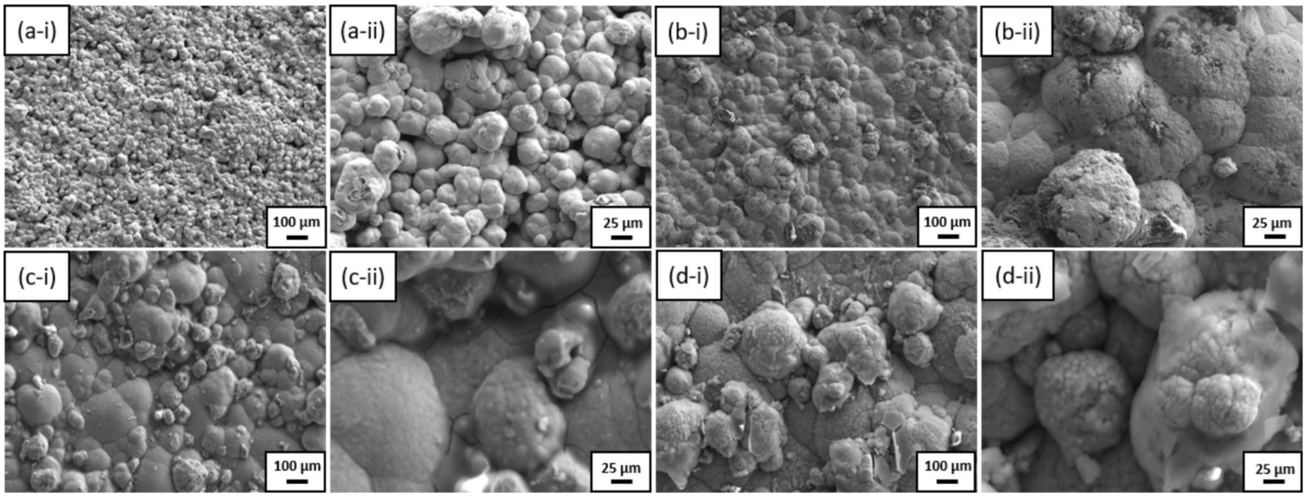

Figure 7 SEM images of co-deposited coatings: **a** Ni + CoCrFeMnNi on copper, **b** Ni + CoCrFeMn on copper, **c** Ni + CoCrFeMnNi on steel, and **d** Ni + CoCrFeMn on steel.

Heat treatment

The final stage of the proposed HEA coating technology involved homogenization by heat treatment. Annealing was conducted for 12 h in a vacuum furnace. The coatings deposited on copper substrates were heated to 920 °C, whereas those on steel substrates were heated to 1120 °C. The surface morphologies of the annealed Ni/CoCrFeMnNi and Ni/CoCrFeMn on copper are shown in Fig. 10a–f, respectively. Both coatings exhibited pronounced surface roughness. In the Ni/CoCrFeMn sample, numerous raised regions were observed (Fig. 10d), some reaching several millimeters in diameter and easily noticeable to the naked eye. These surface irregularities were absent prior to heat treatment.

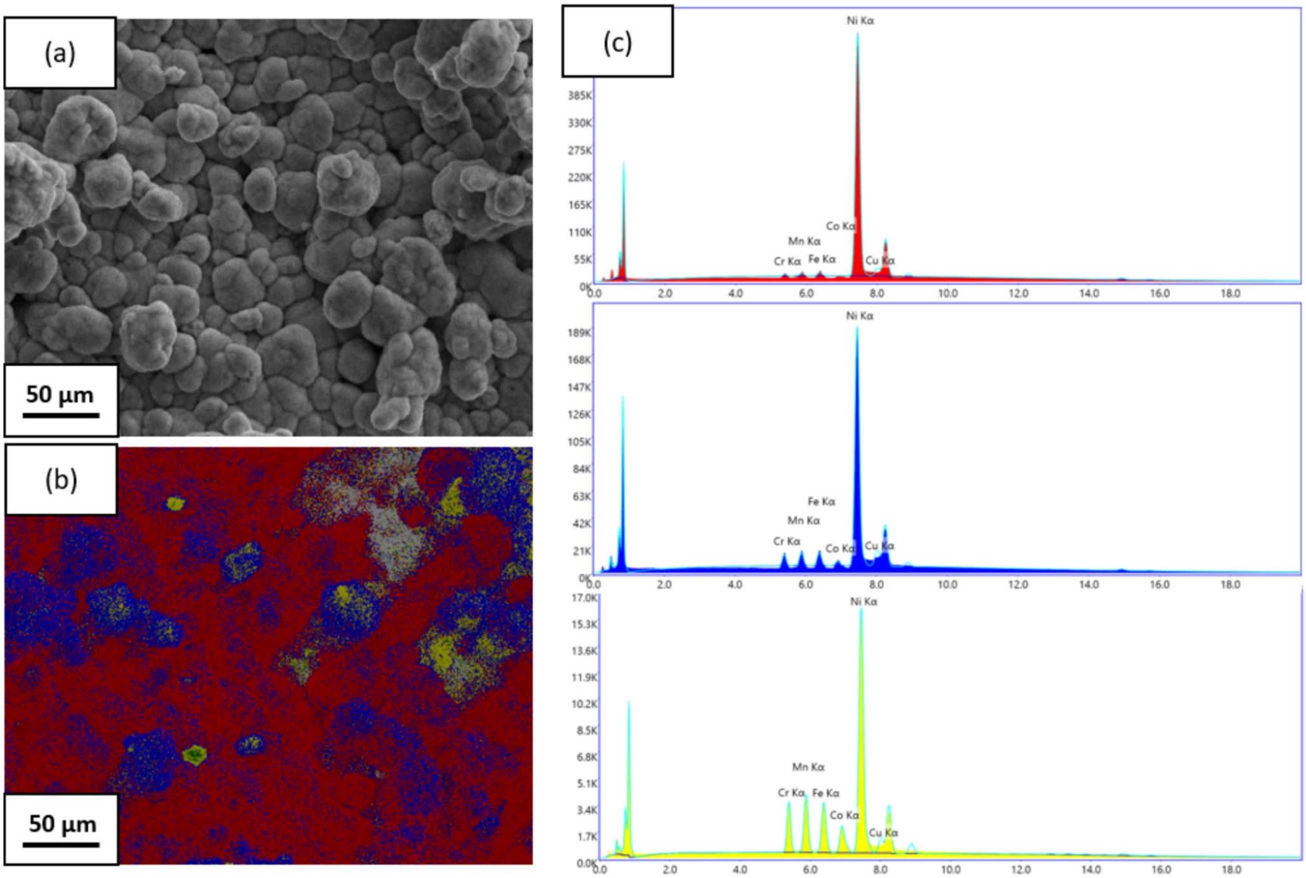

Figure 8 **a** surface SEM image and **b** EDS elemental map of Ni + CoCrFeMnNi on copper, with **c** EDS spectra of each colored area.

SEM observations further revealed a high degree of porosity in both coatings. A clear difference in diffusion behavior was observed between the two systems: while the Ni/CoCrFeMn coating on copper showed nearly complete interdiffusion, the Ni/CoCrFeMnNi coating exhibited incomplete homogenization, with remnants of undissolved HEA particles embedded in the nickel matrix. This behavior can be attributed to the greater thermal stability of CoCrFeMnNi compared with CoCrFeMn.

These results indicate that the combination of HEA particle co-electrodeposition and subsequent annealing can lead to the formation of significant porosity within the coatings. Figure 11 presents the polished surfaces of the Ni/CoCrFeMnNi and Ni/CoCrFeMn on copper. Both samples exhibited pronounced surface nonuniformity characterized by numerous pores and precipitates. Despite the use of different HEA powders during co-deposition, the resulting surface morphologies were largely similar.

Further compositional analysis of the polished surfaces was performed using EDS. As shown in Fig. 12, both Ni/CoCrFeMnNi and Ni/CoCrFeMn coatings on copper exhibited precipitates enriched in chromium and manganese, whereas the distribution of the other constituent elements remained homogeneous throughout the surface.

The microstructures of the coatings were further analyzed on polished cross-sections. Figures 13 and 14 present the cross-sectional SEM images, EDS elemental maps, and line scans of the Ni/CoCrFeMnNi and Ni/CoCrFeMn coatings on copper, respectively. In both cases, the previously observed porosity (Fig. 11) and precipitates were clearly visible. The formation of chromium- and manganese-rich precipitates resulted in local depletion of these elements in the surrounding regions of the coating. Cross-sectional analysis indicated that these precipitates correspond to HEA particles that did not fully dissolve into the nickel matrix during annealing, most likely because of the annealing temperature being insufficient to achieve complete

Figure 9 XRD patterns of co-deposited Ni + CoCrFeMnNi coating on copper.

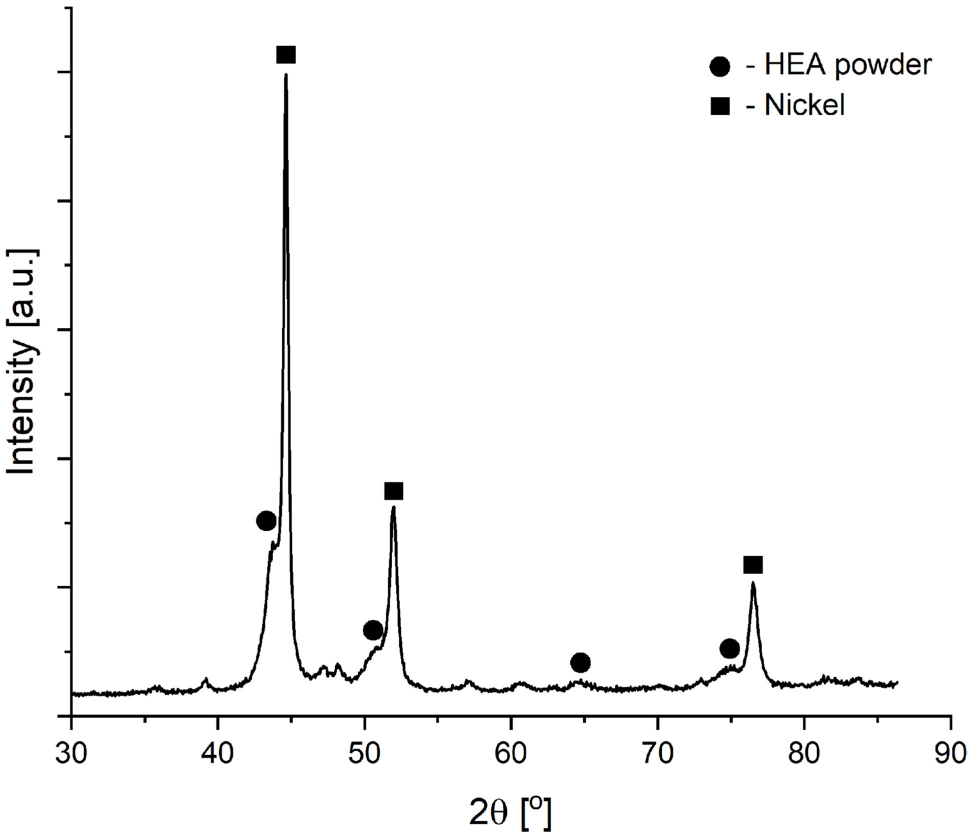

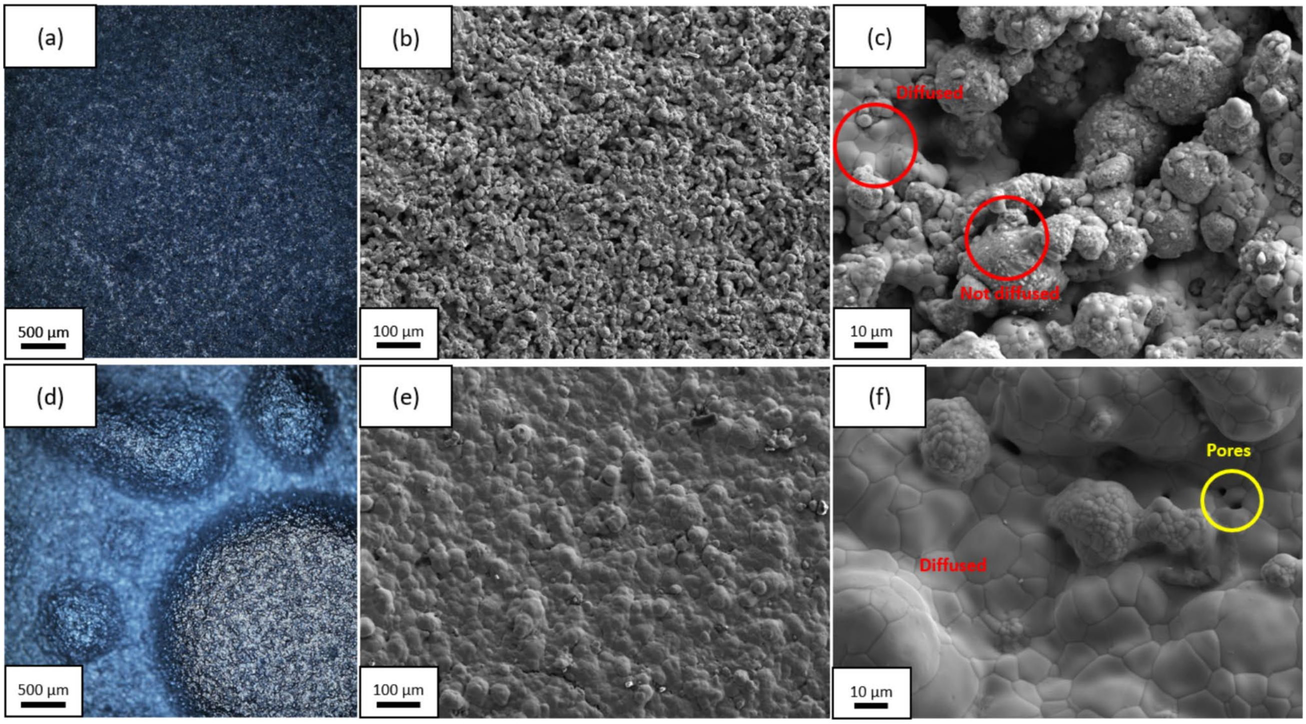

Figure 10 **a**, **b** Optical micrographs and **b**, **c**, **e**, **f** SEM images of sample surfaces after annealing at 920 °C for 12 h: **a–c** Ni/CoCrFeMnNi on copper and **d–f** Ni/CoCrFeMn on copper.

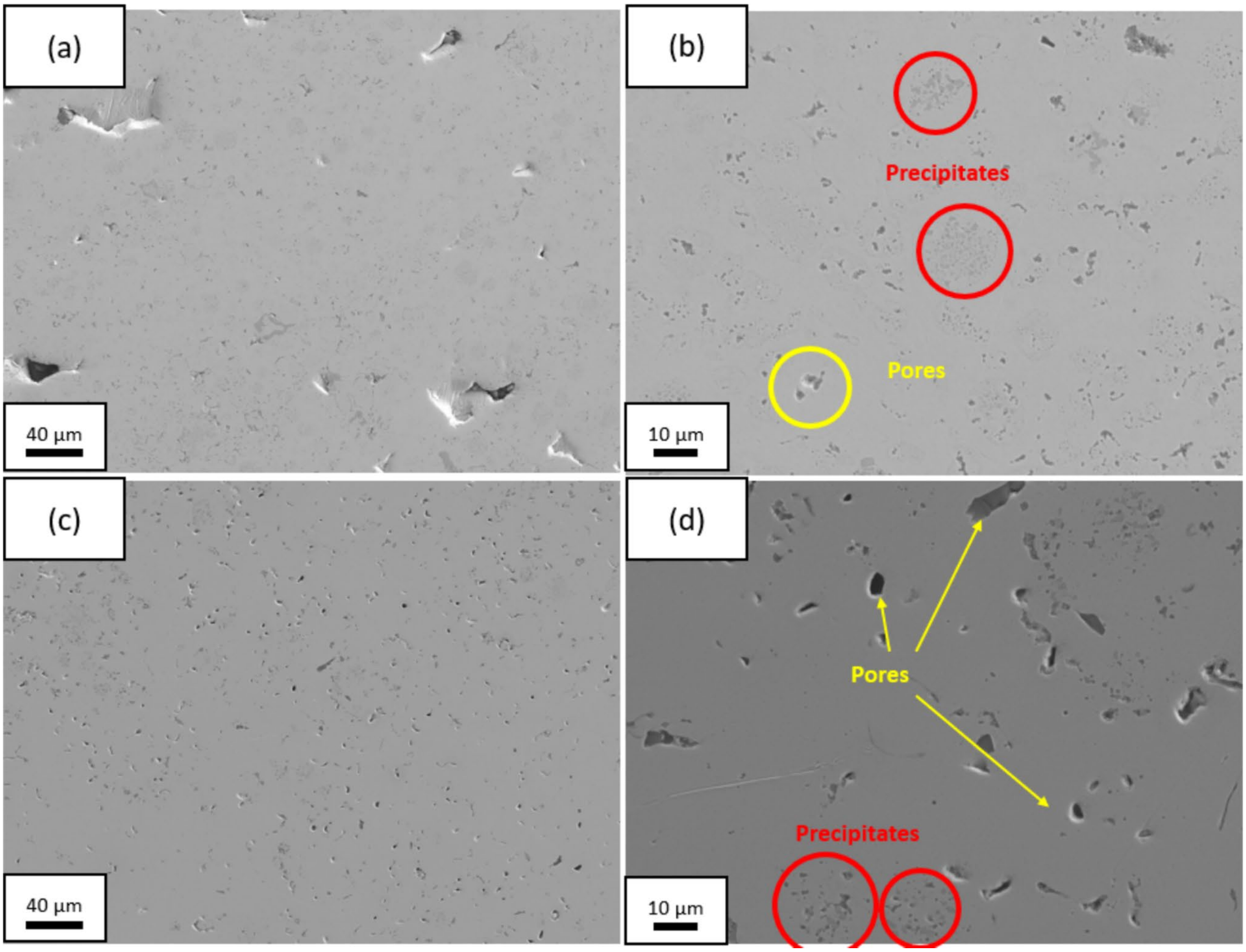

Figure 11 Surface SEM images of annealed samples after polishing: **a**, **b** Ni/CoCrFeMnNi on copper and **c**, **d** Ni/CoCrFeMn on copper.

homogenization. The heat treatment also promoted mutual diffusion between the nickel coating and the copper substrate. This interdiffusion is consistent with the complete solubility of nickel and copper, their similar lattice constants (3.5238 and 3.615 Å, respectively), and their common FCC crystal structure. The absence of a distinct interface between the coating and substrate, resulting from the interdiffusion, demonstrates strong metallurgical bonding and good adhesion.

Figure 15 shows the surface morphologies of the Ni/CoCrFeMnNi and Ni/CoCrFeMn coatings on steel after homogenizing heat treatment for 12 h. These samples were annealed at a higher temperature (1120 °C) than those deposited on copper; nevertheless, similar to the coatings on copper, the coatings on steel also exhibited pronounced roughness and porosity. Numerous raised regions, clearly visible to the naked eye, were present on both Ni/CoCrFeMnNi and Ni/CoCrFeMn coatings (Fig. 15a, b). SEM analysis revealed complete interdiffusion for both coatings (Fig. 15c–f), with no detectable remnants of the precursor HEA particles, likely due to the higher annealing temperature applied in this case.

Figure 16 shows the polished surfaces of the Ni/CoCrFeMnNi and Ni/CoCrFeMn coatings on steel. Both samples exhibited similar appearances, characterized by a largely homogeneous microstructure with only a few pores and precipitates visible (Fig. 16a, b, d, and e). The higher annealing temperature effectively reduced porosity and promoted further homogenization of the coating. However, isolated regions with increased porosity were still observed (Fig. 16c and f).

The surface elemental compositions of the Ni/CoCrFeMnNi and Ni/CoCrFeMn coatings on steel were

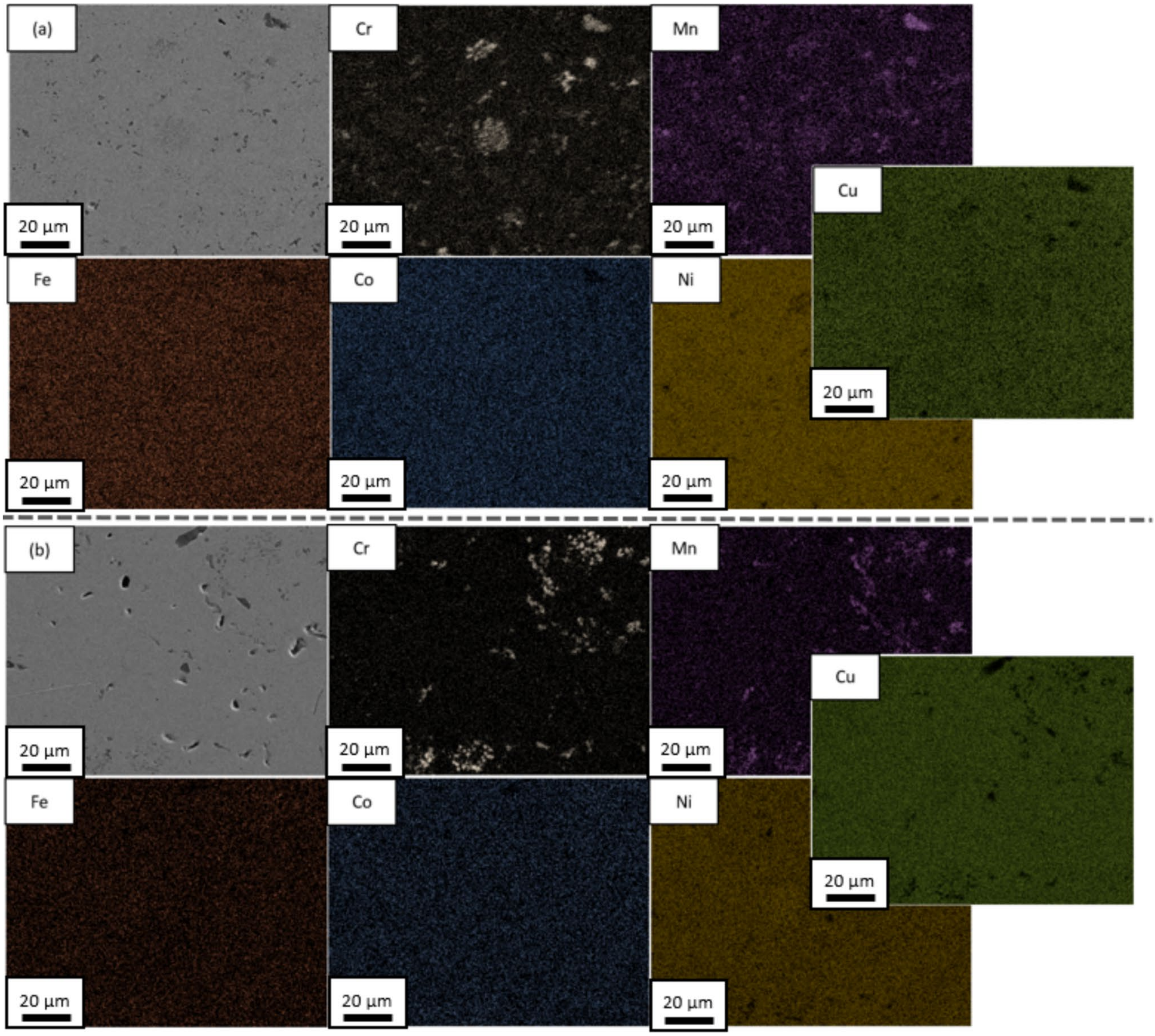

Figure 12 EDS elemental maps of annealed sample surfaces after polishing: **a** Ni/CoCrFeMnNi on copper and **b** Ni/CoCrFeMn on copper.

examined using EDS. Figure 17**a** and **b** present the corresponding elemental maps. Both coatings exhibited largely homogeneous elemental distribution, with only a small number of chromium- and manganese-rich precipitates.

Figures 18 and 19 present the cross-sectional analyses of the Ni/CoCrFeMnNi and Ni/CoCrFeMn on steel, respectively. Both coatings exhibited more homogeneous microstructures compared with those deposited on copper. The higher annealing temperature (1120 °C) promoted pore closure and facilitated more complete homogenization of the coatings, with no undissolved precursor particles detected. Pronounced interdiffusion between the steel substrate and coating was observed, with nickel diffusing deeply into the substrate and iron diffusing into the coating. The absence of a sharp interface between the coating and substrate—resulting from this extensive interdiffusion—indicates strong metallurgical bonding and good adhesion.

Figures 20 and 21 show the results of scratch tests analysis for the Ni/CoCrFeMnNi and Ni/CoCrFeMn

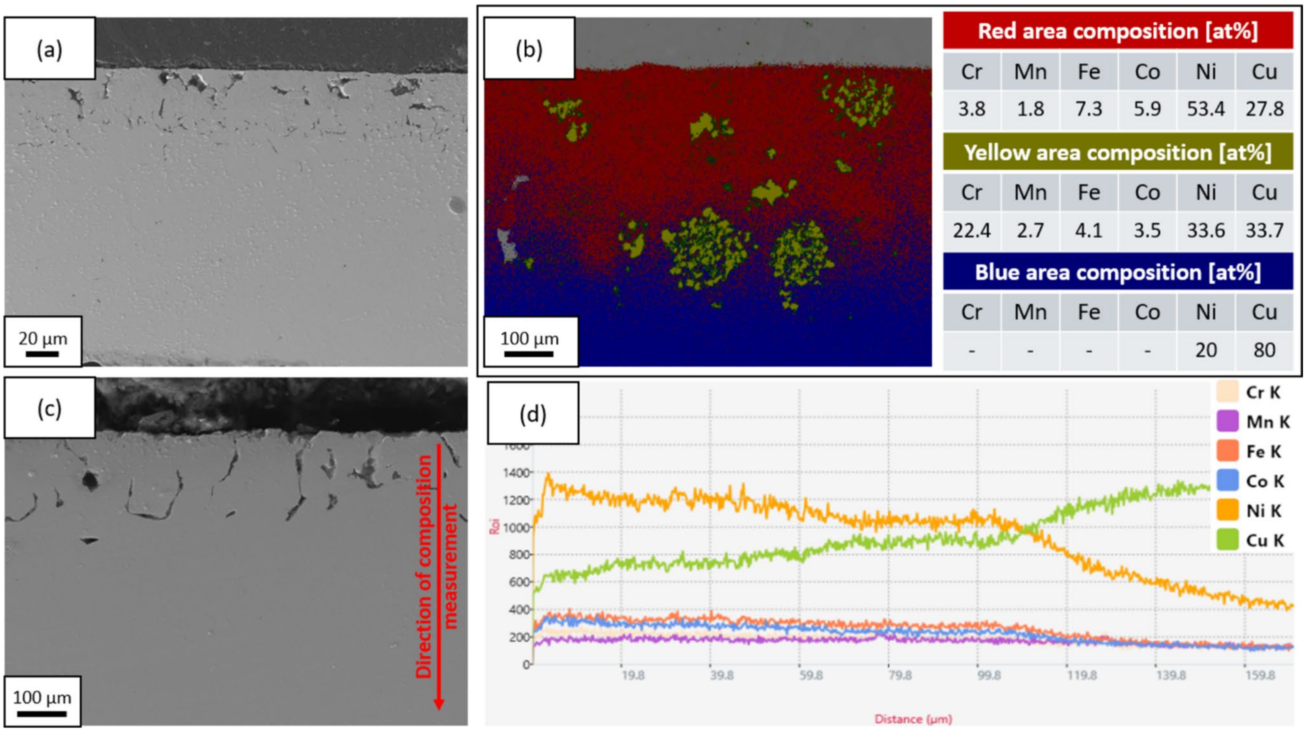

Red area composition [at%]

Cr	Mn	Fe	Co	Ni	Cu
3.8	1.8	7.3	5.9	53.4	27.8

Yellow area composition [at%]

Cr	Mn	Fe	Co	Ni	Cu
22.4	2.7	4.1	3.5	33.6	33.7

Blue area composition [at%]

Cr	Mn	Fe	Co	Ni	Cu
-	-	-	-	20	80

Figure 13 Cross-sectional analysis of the annealed Ni/CoCrFeMnNi coating on copper after cutting and polishing: **a**, **c** SEM images; **b** EDS elemental map with corresponding chemical compositions of the marked areas; and **d** elemental composition profiles as a function of depth from the coating surface.

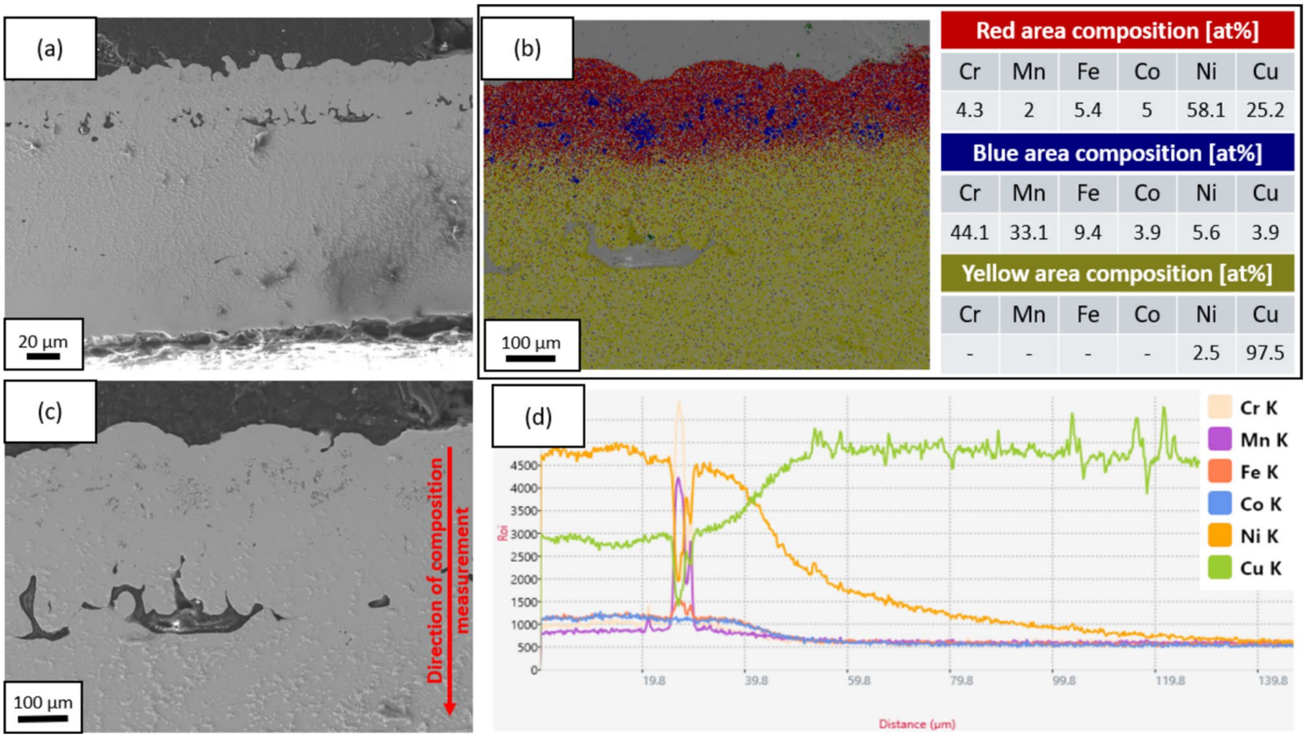

Red area composition [at%]

Cr	Mn	Fe	Co	Ni	Cu
4.3	2	5.4	5	58.1	25.2

Blue area composition [at%]

Cr	Mn	Fe	Co	Ni	Cu
44.1	33.1	9.4	3.9	5.6	3.9

Yellow area composition [at%]

Cr	Mn	Fe	Co	Ni	Cu
-	-	-	-	2.5	97.5

Figure 14 Cross-sectional analysis of the annealed Ni/CoCrFeMn coating on copper after cutting and polishing: **a**, **c** SEM images; **b**EDS elemental map with corresponding chemical compositions of the marked areas; and **d** elemental composition profiles as a function of depth from the coating surface.

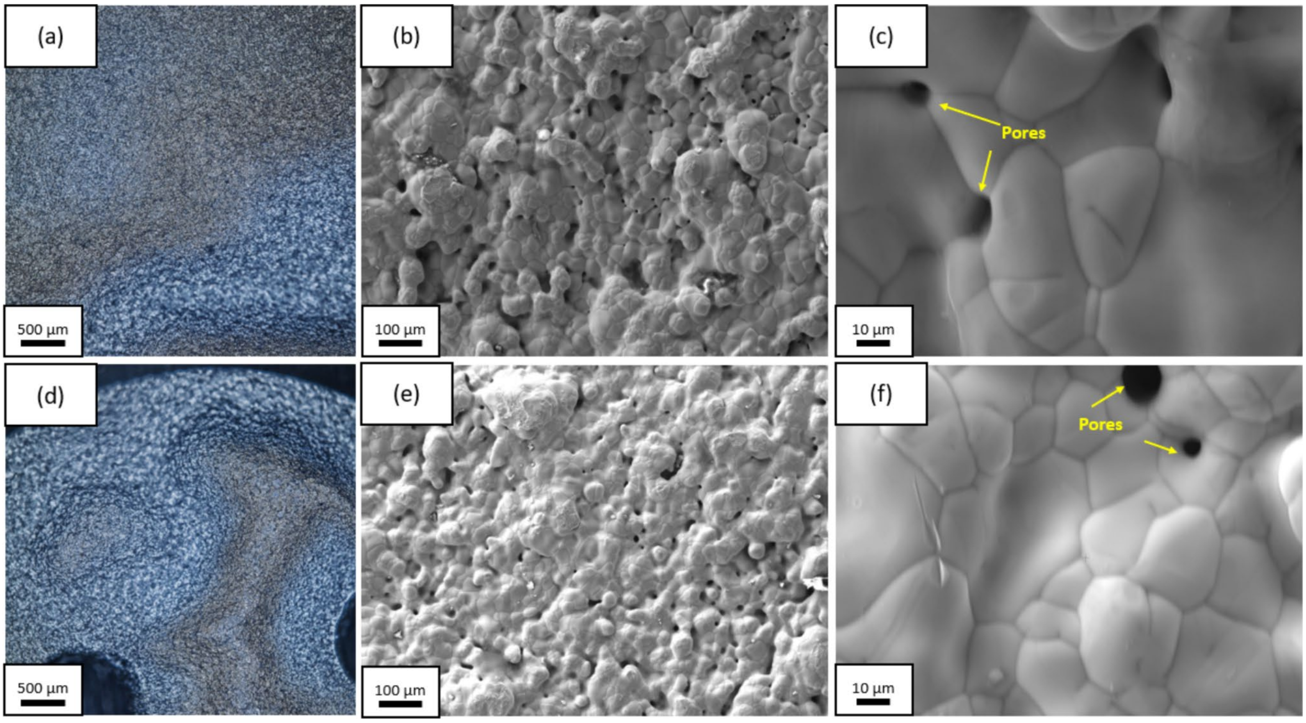

Figure 15 **a**, **d** Optical micrographs and **b**, **c**, **e**, **f** SEM images of sample surfaces after annealing at 1120 °C for 12 h: **a–c** Ni/CoCrFeMnNi on steel and **d–f** Ni/CoCrFeMn on steel.

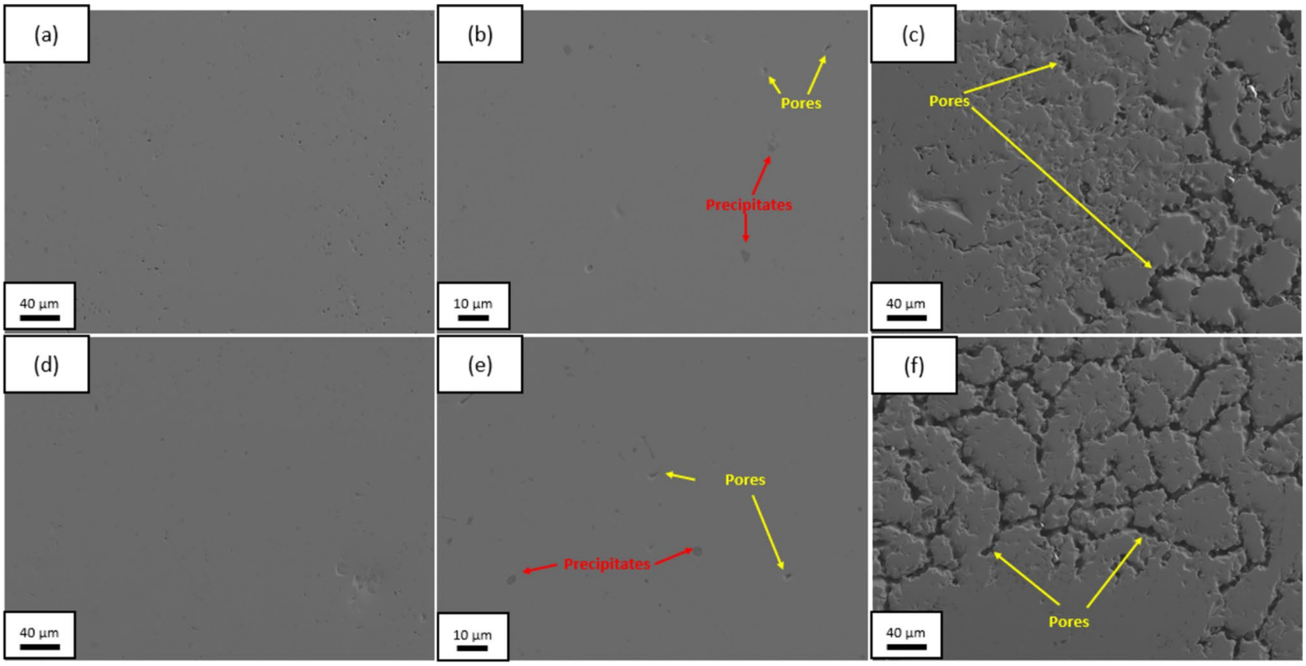

Figure 16 Surface SEM images of the annealed coatings after polishing: **a–c** Ni/CoCrFeMnNi on steel and **d–f** Ni/CoCrFeMn on steel. Both coatings exhibit predominantly homogeneous microstructures as a result of high-temperature annealing, with only isolated regions showing increased porosity or residual precipitates.

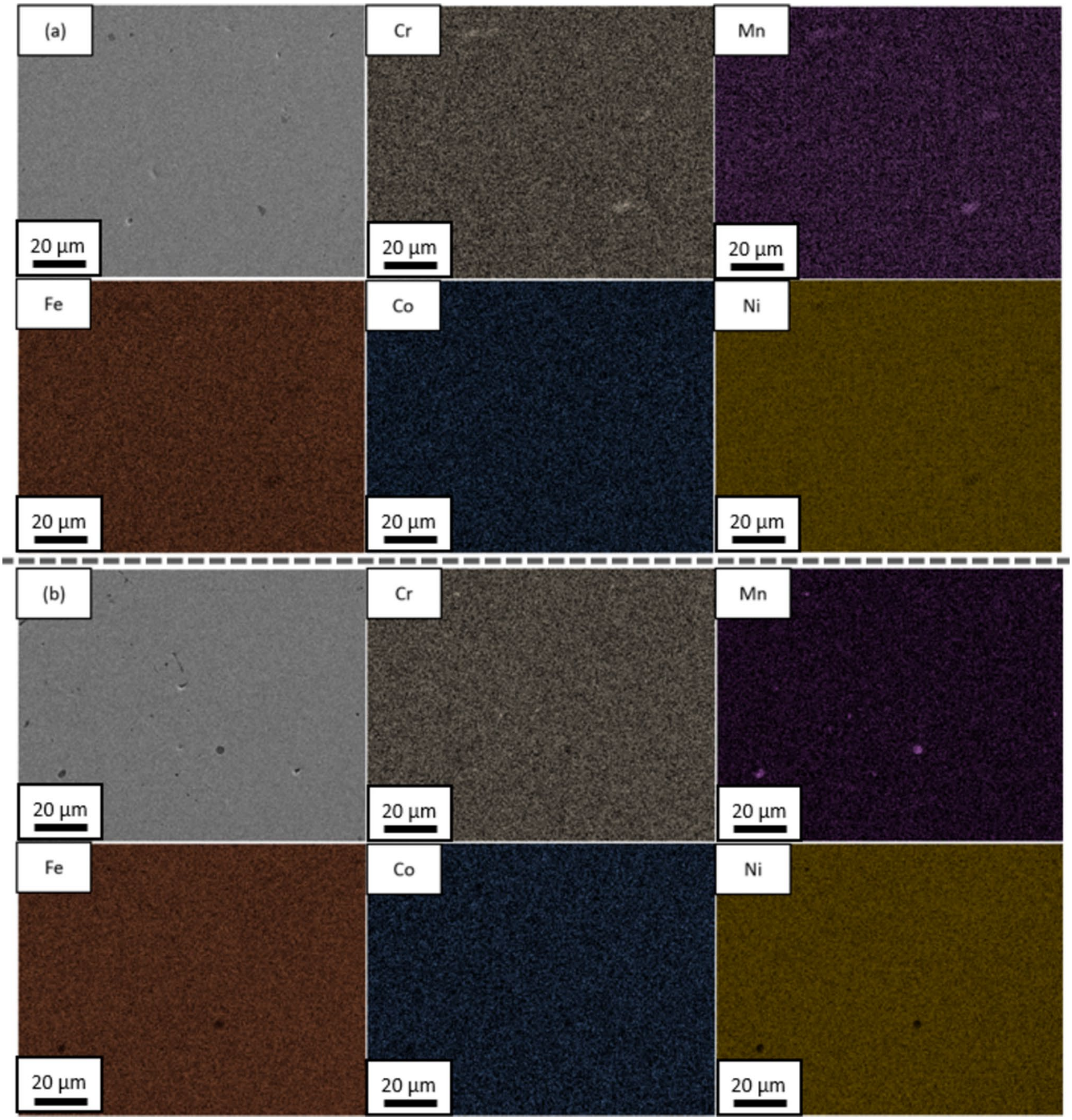

Figure 17 EDS elemental maps of annealed sample surfaces after polishing: **a** Ni/CoCrFeMnNi on steel and **b** Ni/CoCrFeMn on steel.

coating on steel, respectively. For both coatings, no visible cracking or delamination was observed, during the entire scratch test, plastic deformation was observed, indicating strong adhesion to the substrate. This is attributed to the mutual diffusion of coating and substrate during the heat treatment. Notably, the penetration depth during scratching was significantly smaller for the sample prepared with CoCrFeMnNi powder (Fig. 21), which is ascribed to compositional differences between the two alloys and the slightly higher hardness of Ni/CoCrFeMnNi coating.

Figure 22 presents the XRD patterns of the four coatings. For the samples deposited on steel, a

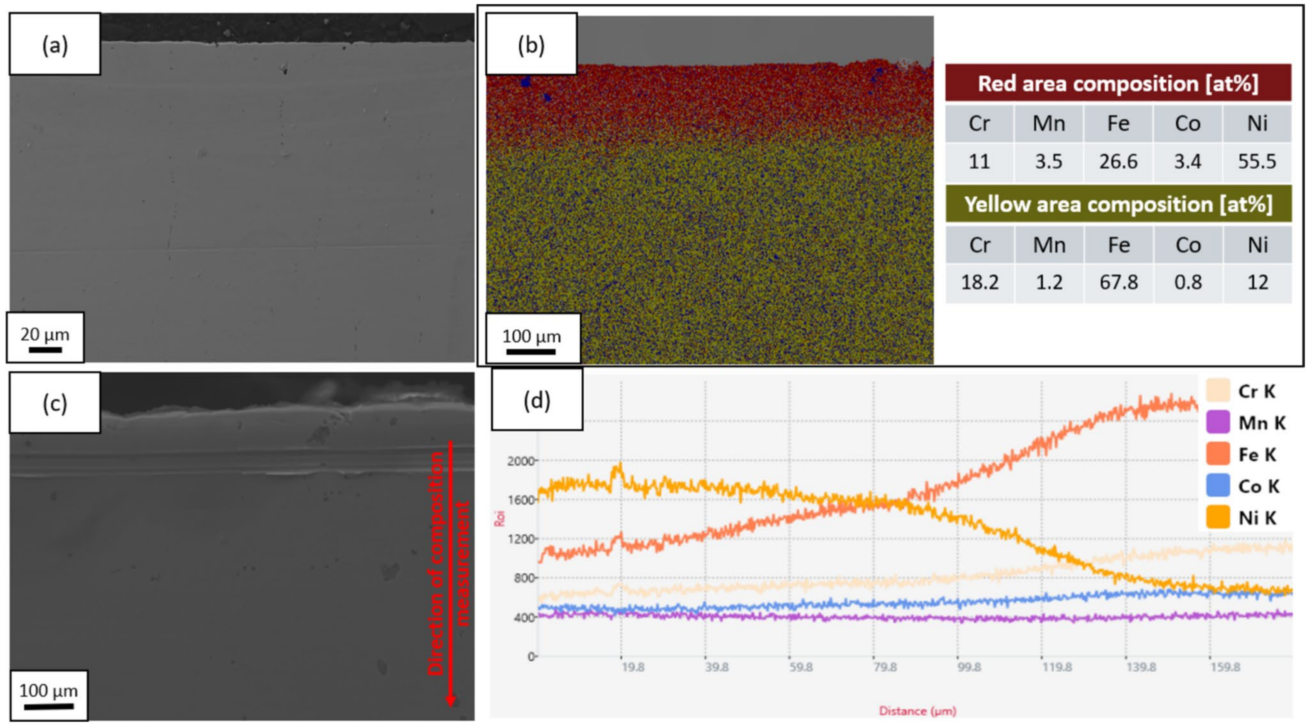

Red area composition [at%]				
Cr	Mn	Fe	Co	Ni
11	3.5	26.6	3.4	55.5

Yellow area composition [at%]				
Cr	Mn	Fe	Co	Ni
18.2	1.2	67.8	0.8	12

Figure 18 Cross-sectional analysis of the annealed Ni/CoCr-FeMnNi coating on steel after cutting and polishing: **a**, **c** SEM images; **b** EDS elemental map with corresponding chemical compositions of the marked areas; and **d** elemental composition profiles as a function of depth from the coating surface.

single-phase FCC solid solution was observed, which can be attributed to the higher annealing temperature applied in their processing. In contrast, the coatings deposited on copper exhibited additional diffraction peaks alongside the FCC phase. The additional reflections can be attributed to manganese- and chromium-rich metallic phases, which remained in the coating due to incomplete diffusion of these elements, as also confirmed by the EDS analysis EDS (Fig. 13 and 14). The presence of such peaks suggest that the annealing was insufficient to fully homogenize all manganese and chromium rich regions into the FCC solid solution, unlike in the case of samples annealed at the higher temperature (1120 °C). The additional reflections are probably associated with the formation of Mn-Cr oxide phases and Mn-Cr σ-type intermetallic phase.

Nanoindentation measurements were conducted at maximum loads of 10 and 50 mN, and the average hardness values obtained after annealing are summarized in Table 3. Higher nanohardness values recorded at the lower load of 10 mN are consistent with the indentation size effect, whereas the lower values obtained at 50 mN may reflect a larger influence of compositional gradients and substrate effects [33–37]. The load-dependent hardness response may also be affected by the complex microstructure of the coatings, including solute-induced lattice distortion, grain boundaries, and, in the case of copper-based samples, residual phase boundaries associated with incomplete homogenization. Although porosity was observed in the coatings, its direct influence on the hardness values is expected to be limited, as the indentation sites were carefully selected away from visible pores and the indent sizes were much smaller than the average pore diameter. Moreover, the same trend of reduced hardness at higher load was observed for the steel-based samples, despite their lower porosity, indicating that the measured load dependence is primarily related to indentation mechanics and substrate effects Badanie wpływu materiału i warunków pracy na ewolucję sprawności oraz zużycie przekładni zębatych wykonanych techniką FDM.

The highest nanohardness value of approximately 6.25 GPa was obtained for the Ni/CoCrFeMnNi coating on copper. This value was significantly higher than those of the remaining samples, whose hardness

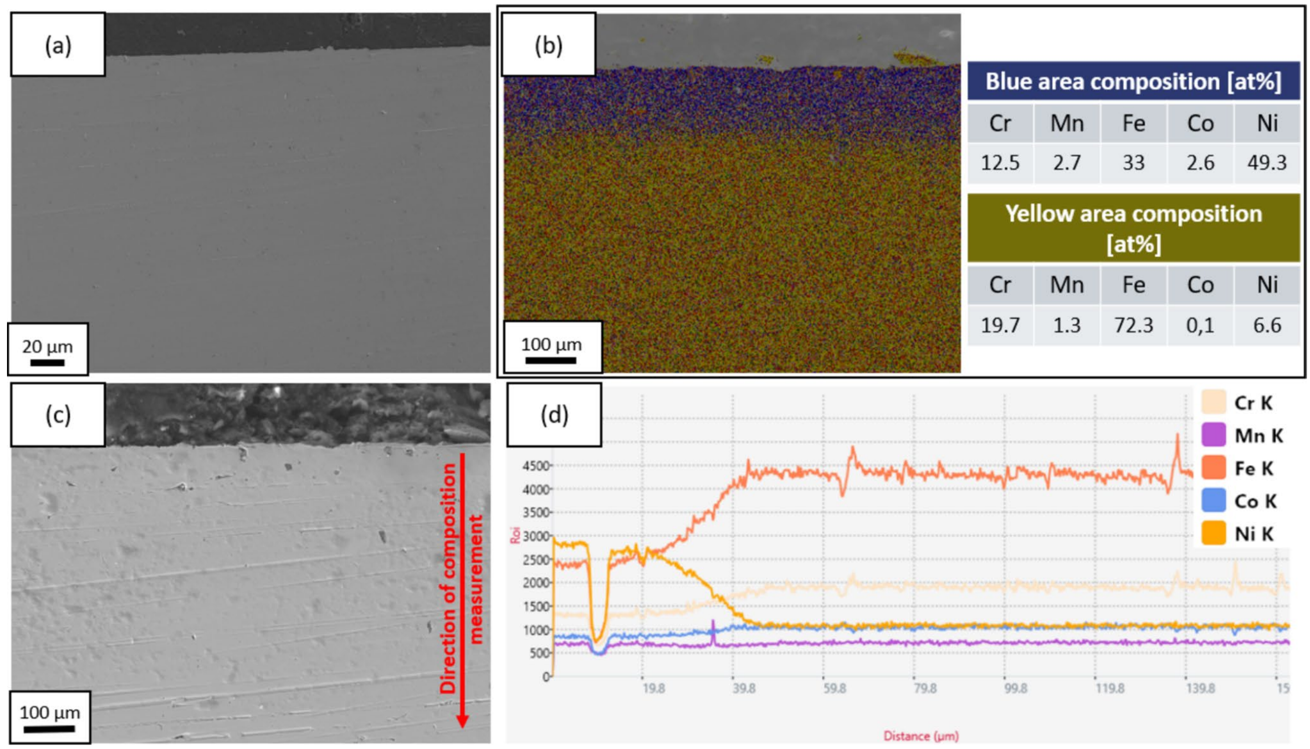

Blue area composition [at%]				
Cr	Mn	Fe	Co	Ni
12.5	2.7	33	2.6	49.3

Yellow area composition [at%]				
Cr	Mn	Fe	Co	Ni
19.7	1.3	72.3	0,1	6.6

Figure 19 Cross-sectional analysis of the annealed Ni/CoCr-FeMn coating on steel after cutting and polishing: **a**, **c** SEM images; **b** EDS elemental map with corresponding chemical compositions of the marked areas; and **d** elemental composition profiles as a function of depth from the coating surface.

values were close to 4 GPa. The average hardness values of all prepared coatings were markedly higher than that reported for bulk CoCrFeMnNi prduced by arc melting and annealing (2.5 ± 0.04 GPa) [38], but comparable to that of bulk CoCrFeMnNi processed by high pressure torsion (6.5 ± 0.04 GPa). In contrast, the average hardness values were significantly lower than that of magnetron-sputtered CoCrFeMnNi (7.9 ± 0.4 GPa) [39], indicating that further process optimization is still required. The higher hardness observed for coatings on copper compared with those on steel can be attributed primarily to the strengthening effect of the second phase (undissolved precursor particles) and the fact that the coatings deposited on steel were annealed at higher temperatures for the same duration, which promoted grain growth and stress relaxation, thereby reducing their mechanical strength. Additionally, substantial diffusion of copper into the coating was detected, which may have contributed to the strengthening through lattice distortion associated with the incorporation of a sixth element. Notably, coatings prepared using CoCrFeMnNi powder exhibited higher hardness compared to those produced with CoCrFeMn powder. This difference is attributed to compositional effects, particularly the higher nickel content in coatings derived from the CoCrFeMnNi-based suspensions.

Discussion

Producing thick high-entropy alloy coatings with high reliability and strong adhesion to the substrate remains both challenging and costly, which underscores the need for alternatives to conventional fabrication methods. In this study, we take the first steps toward proposing a new approach for manufacturing HEA coatings by combining mechanical alloying, electrochemical co-deposition, and subsequent homogenizing heat treatment. Electrochemical techniques offer several advantages: they are relatively simple, cost-effective, and compatible with the deposition of coatings on components with complex geometries. Moreover, the necessary equipment is widely available in industrial settings. Additional benefits include low consumption of raw materials and

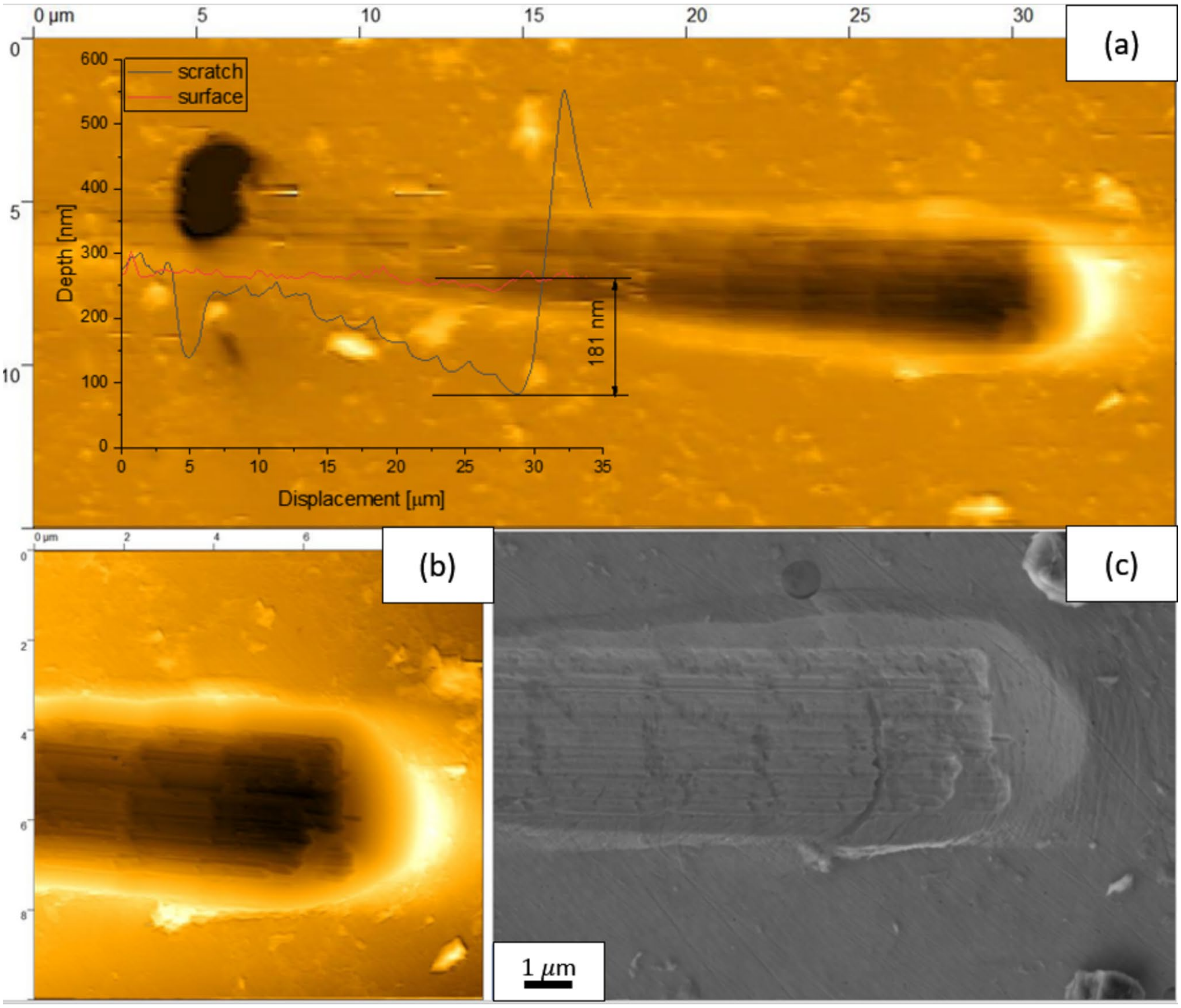

Figure 20 Representative curves of scratch depth and penetration depth determined by scratch test and AFM **a**, **b** with SEM **c** images of surface morphology of the corresponding scratch on annealed Ni/CoCrFeMnNi on steel.

energy, low operating temperatures, short synthesis times, and straightforward scalability [13–15].

Electrochemically deposited coatings are widely used in industry, and the ability to readily fabricate high entropy alloy coatings opens the possibility of employing them even in extreme environments, such as the space applications or nuclear systems. However, the electrodeposition of HEAs—comprising five or more elements – remains highly challenging due to the differing reduction kinetics and preferential deposition tendencies of the individual components [16, 17]. The co-deposition of metals requires a deeper understanding of both thermodynamics and kinetics, as multi-component electrodeposition is inherently more complex than the deposition of single metals or even binary alloys [40, 41]. In practice, electrodeposition processes face numerous difficulties, including controlling composition, avoiding preferential deposition, and ensuring uniformity—challenges that become even more pronounced during industrial-scale processing and scale-up.

Another challenge arises when attempting to electrodeposit elements with very low reduction potentials, such as aluminium or titanium. In aqueous electrolytes, water reduction to hydrogen dominates, making the electrodeposition of these

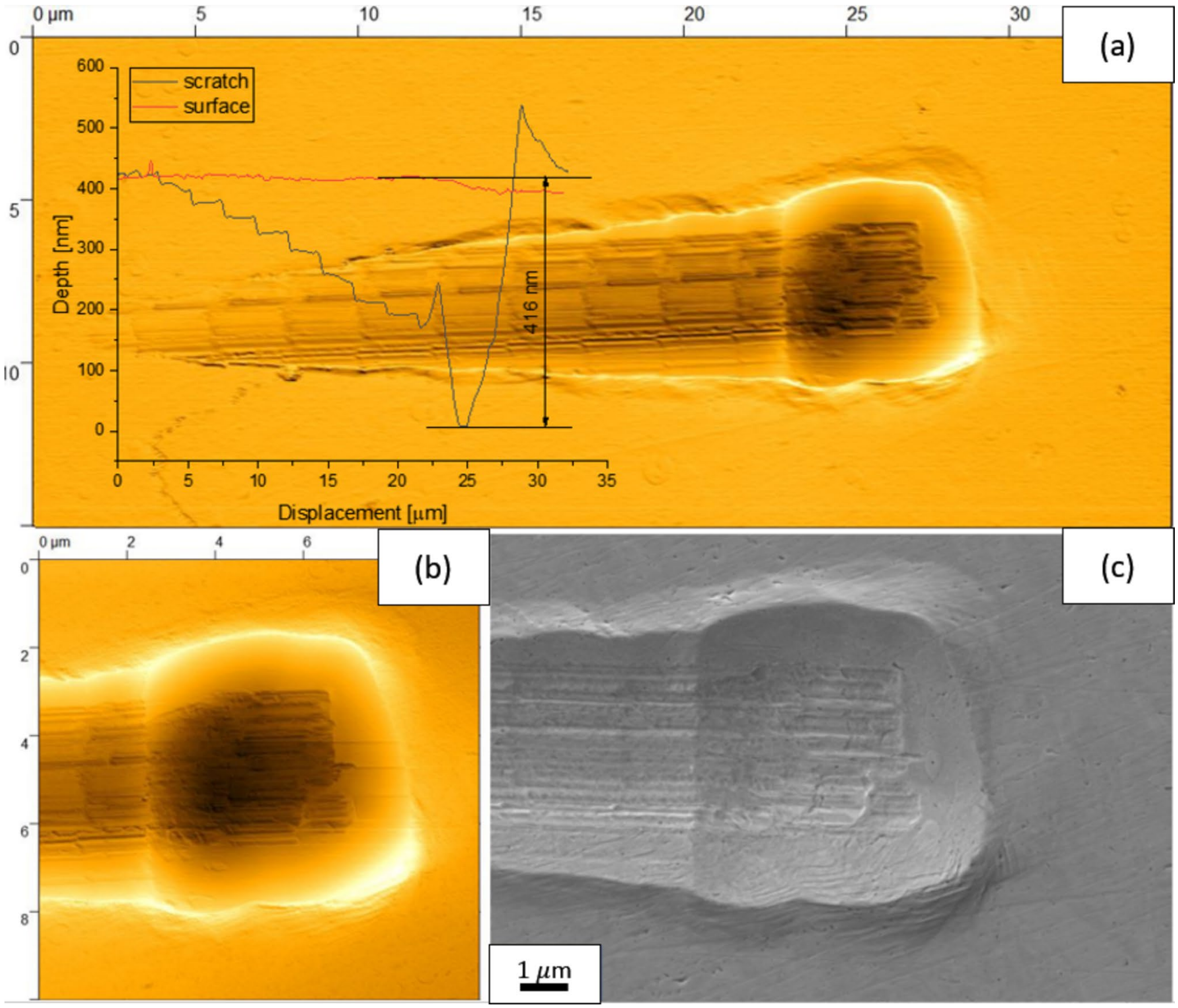

Figure 21 Representative curves of scratch depth determined by scratch test and AFM **a**, **b** with SEM **c** images of surface morphology of the corresponding scratch on annealed Ni/CoCrFeMn on steel.

metals thermodynamically impossible. As a result, elements such as Ti and Al cannot be electrodeposited from aqueous solutions; instead, alternative media—most commonly molten salts—are required [42, 43]. However, these non-aqueous systems often demand highly controlled and challenging operating conditions, further complicating their practical use.

Although suitable methods exist for the electrochemical deposition of individual elements such as Ti or Al, attempting to fabricate coatings composed of many elements (including the above mentioned low-potential metals) introduces substantial difficulties. As the number of components increases, so that the risk that no common set of electrochemical conditions can be identified under which all ions can be simultaneously reduced. The method proposed in this work is designed to overcome this limitation. It requires only one element to possess electrodeposition parameters compatible with aqueous processing; the remaining constituents are introduced into the bath as pre-alloyed metallic powders produced via mechanical alloying. This approach eliminates the need to co-reduce multiple metal ions, thereby greatly simplifying the deposition process. Additionally, it becomes feasible to easily co-electrodeposit many components from aqueous solutions, which

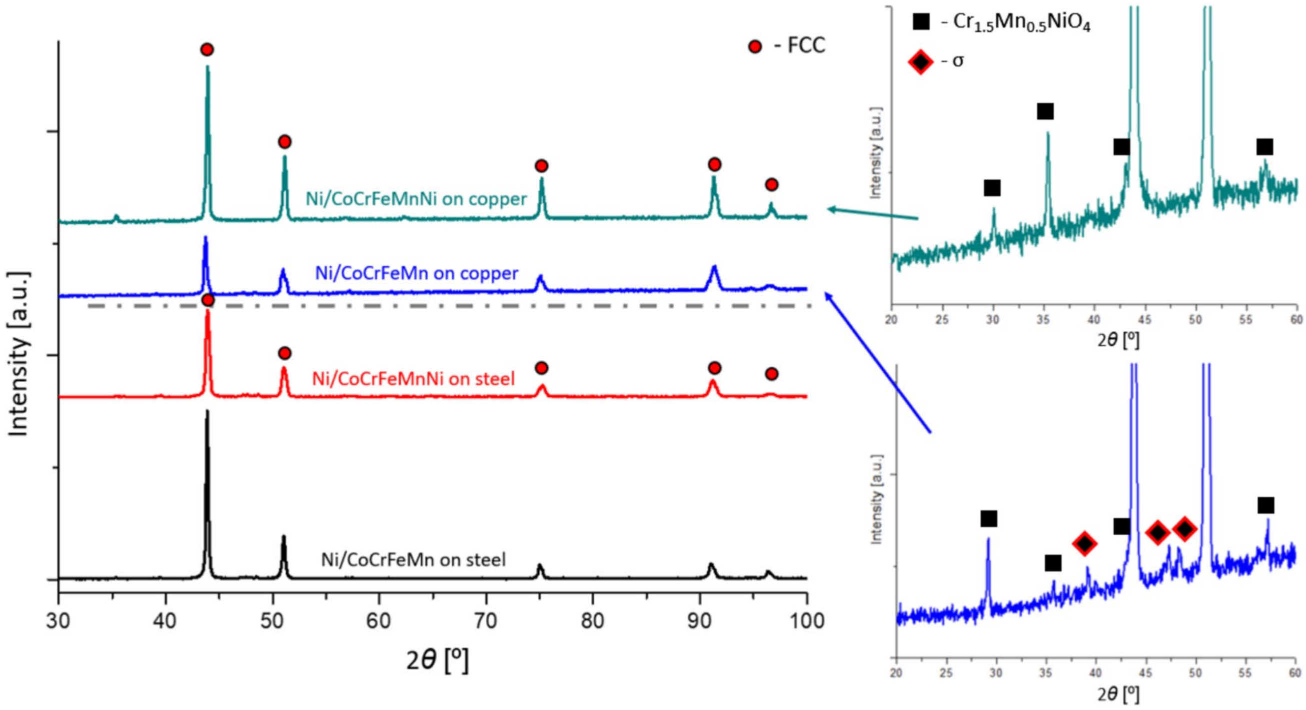

Figure 22 XRD patterns after annealing.

Table 3 Nanohardness of annealed samples

Nanohardness [GPa]				
	Ni/CoCrFeMnNi on copper	Ni/CoCrFeMn on copper	Ni/CoCrFeMnNi on steel	Ni/CoCrFeMn on steel
10 mN	6.25 ± 0.16	3.38 ± 0.43	4.42 ± 0.56	3.42 ± 0.29
50 mN	3.1 ± 0.23	3.13 ± 0.29	2.44 ± 0.18	2.28 ± 0.25

further reduces the cost and toxicity of the process compared to for example, baths based on organic solvents.

Although the proposed approach significantly simplifies the co-electrodeposition of multi-component systems, it also introduces new challenges. Coatings obtained in this way often require heat treatment at high temperatures to achieve compositional uniformity (homogenization). This requires the use of substrates that are resistant to high temperatures, but at the same time annealing improves adhesion through the diffusion of components between the coating and the substrate, eliminating the risk of delamination. Efficient incorporation of alloy powder during co-electrodeposition further depends on proper electrolyte agitation. Factors such as particle shape and size, as well as electrode geometry, play a crucial role in ensuring uniform powder transport and deposition.

Despite these challenges, the advantages of the proposed method, when process parameters are refined, may enable the broader adoption of HEA coatings in demanding applications, including space technologies, nuclear power plants or even the rapid production of HEA based electrode materials for Li-ion batteries. In such cases, numerous compositional variants can be explored without the need to design and refine a separate, complex electrolyte bath for each alloy system, greatly accelerating materials development.

HEA particle characteristics

Although the effects of particle size and shape on the co-deposition process were not specifically addressed in this study, these factors may significantly affect the final product. Despite differences in the shape and size of the CoCrFeMnNi and CoCrFeMn powder particles, no specific differences in the co-deposition process were identified as being attributed to these characteristics. Conductive particles such as those used here are more readily incorporated into the coating because they are attracted to the cathode and act as additional nucleation sites during electrodeposition. While this can increase surface roughness and promote pore formation, it also enhances the integration of the particles into the nickel matrix.

The use of nonconductive particles, such as high-entropy ceramics, may result in smoother surfaces [44]. Particle size can also influence the final product; however, there is no consistent trend of the size–property relationship [45–47], and this should be evaluated on a case-by-case basis. In the present study, the precursor powders exhibited a wide particle-size distribution, ranging from a few micrometers to several hundred micrometers, which may have reduced the amount of powder incorporated into the coating. Previous reports indicate that particles do not attach directly to ones deposited on the cathode surface [48, 49]. Instead, before a new particle can be captured, nickel ions from the solution must first be reduced onto the existing particle surfaces. Consequently, smaller particles have a higher chance of being densely packed, leading to a higher content of particles in the coating.

Effect of hydrogen

The mechanism of nickel electrodeposition from a Watts bath was determined by impedance measurements in study performed by I. Epelboin and R. Wiart [50] which revealed only one inductive loop which has been ascribed to the relaxation of the electrode coverage by an adsorbed intermediate such as (NiOH) and the following reaction mechanism has been suggested:

$$\mathrm{Ni^{2+} + H_2O \rightarrow (NiOH)^+ + \ H^+}$$

$$\mathrm{(NiOH)^+ + }e^- \rightarrow \mathrm{(NiOH)_{ads}}$$

$$\mathrm{(NiOH)_{ads} + (NiOH)^+ + 3}e^- \rightarrow \mathrm{2Ni + 2OH^-}$$

During electrodeposition, hydrogen is produced on the cathode, which negatively affects both the deposition rate and the current efficiency, and can also influence the microstructure causing porosity and properties of the deposited metal. Hydrogen evolution may further promote the adsorption of other components (e.g., hydrides or hydroxides) [51] or, in severe cases, even lead to the delamination of the coating [52]. Furthermore, the reduction of oxygen and water near the cathode can cause pH changes near the electrode, which also disturbs the deposition parameters. A previous study [53] indicated that the deposition of pure nickel consists of the reduction of hydrogen ions, deposition of metallic nickel, and reduction of water. The occurring reactions, referred to as hydrogen evolution reactions (HER), are described as follows:

$$\mathrm{2H_3O^+ + 2}e^- \rightarrow \mathrm{H_2 + 2H_2O}$$

$$\mathrm{2H_2 + 2}e^- \rightarrow \mathrm{H_2 + 2OH^-}$$

Adsorbed hydrogen can be incorporated into the deposit layer, just as hydroxides, which compete with metal deposition process. The contribution of individual reactions depends on the range of the applied potential [54–56].

One strategy to mitigate these effects is to use a degassing or deoxygenating electroplating bath, as used in voltammetry [57], in which dissolved oxygen is removed by purging the solution with an inert gas such as argon or nitrogen.

This aspect is critical, as residual porosity has a significant impact on potential applications in sectors such as the aerospace or nuclear energy. If porosity is not effectively eliminated, the functional performance is substantially compromised. Residual porosity leads to a degradation of corrosion resistance, promoting crevice corrosion, and also affects mechanical properties, including hardness, wear resistance, and fatigue life.

Effect of annealing temperature

The different degree of homogenization observed for coatings on different substrates (copper and steel) and different annealing temperatures (920 and 1120 °C) is caused by the temperature dependence of diffusion during annealing. In our coatings, chemical homogenization is controlled by the mobility of individual elements and their diffusion in nickel matrix, which can be observed due to incomplete diffusion of individual elements in lower temperatures. The diffusion coefficient follows an Arrhenius relationship $D_i = D_i^0 exp(\frac{-E_a}{RT})$, where E_a is activation energy, R – gas constant, T – temperature, indicating that increase in annealing temperature result in a significant increase in atomic mobility. Therefore, samples annealed at higher temperature of 1120 °C are expected to exhibit more complete homogenization, what we observed. In the samples annealed at lower temperatures, the diffusion was not sufficient to fully eliminate local inhomogeneities. As a result we observed areas rich in chromium and manganese after annealing in 920 °C.

Increasing the annealing temperature improved the homogenization of the coatings by promoting more complete dissolution of the precursor HEA particles within the nickel matrix. However, it also accelerated grain growth and facilitated stress relaxation, which reduced hardness of the material, but potentially enhanced its ductility. Therefore, the method described herein offers the possibility of depositing relatively hard composite coatings with some undissolved HEA particles, or more ductile coatings with greater homogeneity. By adjusting the annealing temperature, the mechanical response of the coating can be tailored to meet the requirements of specific applications.

Effect of substrate material

The coatings deposited on copper exhibited higher hardness than those on steel. However, because copper has a significantly lower melting point than nickel and the elements in the HEA powder, it was not possible to reach the optimal annealing temperature, resulting in incomplete homogenization. This resulted in the presence of undissolved particles. Therefore, the proposed method is constrained by the melting temperature of the substrate.

The approach presented in this work combines mechanical alloying, electrochemical co-deposition, and annealing. However, the coating compositions deviated substantially from equimolar, as typically required for HEAs. Hence, further studies are required

Table 4 Chemical composition of prepared materials

Sample	Elements composition	HEA powders (atomic content %)	Nickel matrix (atomic content %)	Precipitation phase (atomic content %)
Sample 1 Ni/CoCrFeMnNi on copper	Co	19.28	5.9	3.5
	Cr	20.09	3.8	22.4
	Fe	20.63	7.3	4.1
	Mn	20.12	1.8	2.7
	Ni	19.88	53.4	33.6
	Cu	–	27.8	33.7
Sample 2 Ni/CoCrFeMnon copper	Co	24.37	5	3.9
	Cr	25.23	4.3	44.1
	Fe	25.01	5.4	9.4
	Mn	25.39	2	33.1
	Ni	–	58.1	5.6
	Cu	–	25.2	3.9
Sample 3 Ni/CoCrFeMnNi on steel	Co	19.28	3.4	–
	Cr	20.09	11	–
	Fe	20.63	26.6	–
	Mn	20.12	3.5	–
	Ni	19.88	55.5	–
	Cu	–	–	–
Sample 4 Ni/CoCrFeMnon steel	Co	24.37	2.6	–
	Cr	25.23	12.5	–
	Fe	25.01	33	–
	Mn	25.39	2.7	–
	Ni	–	49.3	–
	Cu	–	–	–

to tailor the coating composition. Future work should focus on increasing the amount of HEA powder to matrix phase in the electrodeposited coating, which may be achieved through adjustments in stirring intensity, current density, bath hydrodynamics, and overall experimental configuration.

Chemical composition

Table 4 shows the chemical composition of the prepared coatings together with the composition of the powders used for their fabrication. The powders used in this study had equimolar compositions, and two variants were prepared: a five component powder and four component powder without nickel. As expected, slightly lower nickel contents were observed in the coatings produced using the four component powder. However, this decrease was not sufficient, indicating that further optimization of the process is required. Possible approaches to address this issue have been discussed in the previous sections, including the evaluation of the effects of powder particle size and morphology, mixing conditions of the electrodeposition bath, solution stirring rate, cathode geometry, in order to maximize the amount of powder incorporated into the coating during co-electrodeposition. Nevertheless, the obtained results confirm the feasibility of incorporating HEA powder into the coating during co-electrodeposition. This approach significantly simplifies the electrodeposition of HEA based coatings compared with conventional electrodeposition methods based on the simultaneous reduction of multiple metallic ions from a single electrolyte.

Conclusions

The main objective of this study was to evaluate the feasibility of producing HEA coatings by a combination of mechanical alloying, electrochemical co-deposition, and homogenizing heat treatment. Coatings were prepared on different substrates (copper or steel) and with different HEA precursor powders (CoCrFeMnNi or CoCrFeMn). The annealing time was 12 h, and the annealing temperature was 920 °C for copper substrates and 1120 °C for steel substrates. Co-electrodeposition using HEA precursor powders without nickel did not significantly reduce the nickel content in the coating, because most of the nickel in the coating was derived from the electrolyte solution. Using a steel substrate enabled the annealing temperature to be increased to 1120 °C, resulting in better homogenization, lower porosity, and higher grain growth. Annealing at lower temperatures resulted in higher porosity, lower grain growth, and areas with undissolved HEA precursor powder. The highest hardness of approximately 6.25 GPa was obtained for Ni/CoCrFeMnNi on copper at a load of 10 mN, which was related to second-phase strengthening by the undissolved HEA powder.

On behalf of all authors, the corresponding author states that there is no conflict of interest.

Data sets generated during the current study are available from the corresponding author on reasonable request.

Acknowledgements

This work was supported by the National Science Centre in Poland [grant number 2021/41/N/ST5/02920]. The sponsor had no involvement in the study design; in the collection, analysis, or interpretation of data; in the writing of the report; or in the decision to submit the article for publication.

Funding

Narodowe Centrum Nauki, 2021/41/N/ST5/02920, Dariusz M. Jarzabek

References

[1] Yeh JW, Chen SK, Lin SJ, Gan JY, Chin TS, Shun TT, Tsau CH, Chang SY (2004) Nanostructured high-entropy alloys with multiple principal elements: Novel alloy design concepts and outcomes. Adv Eng Mater 6:299–303. https://doi.org/10.1002/adem.200300567

[2] Zhang Y (2019) High-Entropy Materials. Springer, Singapore

[3] George EP, Curtin WA, Tasan CC (2020) High entropy alloys: A focused review of mechanical properties and deformation mechanisms. Acta Mater 188:435–474. https://doi.org/10.1016/j.actamat.2019.12.015

[4] Yeh JW (2006) Recent progress in high-entropy alloys. Ann Chim Sci Matér 31:633–648. https://doi.org/10.3166/acsm.31.633-648

[5] Ayyagari AV, Gwalani B, Muskeri S, Mukherjee S, Banerjee R (2018) Surface degradation mechanisms in precipitation-hardened high-entropy alloys, npj Mater. Degrad. https://doi.org/10.1038/s41529-018-0054-1

[6] Yoosefan F, Ashrafi A, Monir Vaghefi SM, Constantin I (2020) Synthesis of CoCrFeMnNi high entropy alloy thin films by pulse electrodeposition: PART 1: effect of pulse electrodeposition parameters. Met Mater Int 26:1262–1269. https://doi.org/10.1007/s12540-019-00404-1

[7] Zhao H, Zheng Z, Jiang T, Fu L, Akhavan B, Bilek MM, Liu Z (2023) High entropy alloy thin films on SS304 substrates: Evolution of microstructure and interface modulated by energetic condensation in nanoscale. Mater Des 230:111981. https://doi.org/10.1016/j.matdes.2023.111981

[8] Zhang Q, Wang Q, Han B, Li M, Hu C, Wang J (2023) Comparative studies on microstructure and properties of CoCrFeMnNi high entropy alloy coatings fabricated by high-speed laser cladding and normal laser cladding. J Alloys Compd 947:169517. https://doi.org/10.1016/j.jallcom.2023.169517

[9] Jansson A, Medina LZ, Lautrup L, Jansson U (2023) Magnetron sputtering of the high entropy alloy CoCrFeMnNi on 316L: Influence of substrate grain orientations. Surf Coat Technol 466:129612. https://doi.org/10.1016/j.surfcoat.2023.129612

[10] Xiao X, Lin M, Xu C, Zhang J, Liao W-B (2024) An efficient approach to develop and screen out high-entropy alloy composition with high performance for biomedical application. Surf Coat Technol 478:130504. https://doi.org/10.1016/j.surfcoat.2024.130504

[11] Mahaffey J, Vackel A, Whetten S, Melia M, Kustas AB (2022) Structure evolution and corrosion performance of CoCrFeMnNi high entropy alloy coatings produced via plasma spray and cold spray. J Therm Spray Technol 31:1143–1154. https://doi.org/10.1007/s11666-022-01373-5

[12] Zhu Y, Cui J, Guo X, Ren J (2024) Multi-component thin films and coatings. Mater Des 238:112664. https://doi.org/10.1016/j.matdes.2024.112664

[13] Simka W, Puszczyk D, Nawrat G (2009) Electrodeposition of metals from non-aqueous solutions. Electrochim Acta 54:5307–5319. https://doi.org/10.1016/j.electacta.2009.04.028

[14] Wang S, Guo X, Yang H, Dai J, Zhu R, Gong J, Peng L, Ding W (2014) Electrodeposition mechanism and characterization of Ni-Cu alloy coatings from a eutectic-based ionic liquid. Appl Surf Sci 288:530–536. https://doi.org/10.1016/j.apsusc.2013.10.065

[15] Abbott AP, McKenzie KJ (2006) Application of ionic liquids to the electrodeposition of metals. Phys Chem Chem Phys 8:4265–4279. https://doi.org/10.1039/b607329h

[16] Popescu AMJ, Branzoi F, Burada M, Moreno JC, Anastasescu M, Anasiei I, Olaru MT, Constantin V (2023) CoCrFeMnNi high-entropy alloy thin films electrodeposited on aluminum support. Coatings 13:980. https://doi.org/10.3390/coatings13060980

[17] Shojaei Z, Khayati GR, Darezereshki E (2022) Review of electrodeposition methods for the preparation of high-entropy alloys. Int J Miner Metall Mater 29:1683–1696. https://doi.org/10.1007/s12613-022-2439-y

[18] Dong M, Liu P, Wang C, Wang Y, Tang X, He M, Liu J (2024) Microstructure and properties of FeCoNiCr and FeCoNiCrW high entropy alloy coatings by electro-deposition. Intermetallics 175:108492. https://doi.org/10.1016/j.intermet.2024.108492

[19] Dehestani M, Sharafi S, Khayati GR (2022) The effect of pulse current density on the microstructure, magnetic, mechanical, and corrosion properties of high-entropy alloy coating Fe–Co–Ni–Mo–W, achieved through electro co-deposition. Intermetallics 147:107610. https://doi.org/10.1016/j.intermet.2022.107610

[20] Abd El Meguid EA (1997) Morphology and impedance characteristics of nickel electroplating from Watts bath. Mater Trans 38:731–736. https://doi.org/10.2320/matertrans1989.38.731

[21] Mimani T, Mayanna SM, Munichandraiah N (1993) Influence of additives on the electrodeposition of nickel from a Watts bath: a cyclic voltammetric study. J Appl

Electrochem 23(4):339–345. https://doi.org/10.1007/BF00296689

[22] Li X, Bhushan B (2002) A review of nanoindentation continuous stiffness measurement technique and its applications. Mater Charact 48:11–36. https://doi.org/10.1016/S1044-5803(02)00192-4

[23] Oliver WC, Pharr GM (1992) An improved technique for determining hardness and elastic modulus using load and displacement sensing indentation experiments. J Mater Res 7:1564–1583. https://doi.org/10.1557/JMR.1992.1564

[24] Guo S, Liu CT (2011) Phase stability in high entropy alloys: Formation of solid-solution phase or amorphous phase. Prog Nat Sci Mater Int 21:433–446. https://doi.org/10.1016/S1002-0071(12)60080-X

[25] Zhang Y, Zhou YJ, Lin JP, Chen GL, Liaw PK (2008) Solid-solution phase formation rules for multi-component alloys. Adv Eng Mater 10:534–538. https://doi.org/10.1002/adem.200700240

[26] Xie Y, Cheng H, Tang Q, Chen W, Chen W, Dai P (2018) Effects of N addition on microstructure and mechanical properties of CoCrFeNiMn high entropy alloy produced by mechanical alloying and vacuum hot pressing sintering. Intermetallics 93:228–234. https://doi.org/10.1016/j.intermet.2017.09.013

[27] Zhu ZG, Ma KH, Wang Q, Shek CH (2016) Compositional dependence of phase formation and mechanical properties in three CoCrFeNi-(Mn/Al/Cu) high entropy alloys. Intermetallics 79:1–11. https://doi.org/10.1016/j.intermet.2016.09.003

[28] Ji W, Wang W, Wang H, Zhang J, Wang Y, Zhang F, Fu Z (2015) Alloying behavior and novel properties of CoCrFeNiMn high-entropy alloy fabricated by mechanical alloying and spark plasma sintering. Intermetallics 56:24–27. https://doi.org/10.1016/j.intermet.2014.08.008

[29] Yu PF, Zhang LJ, Cheng H, Zhang H, Ma MZ, Li YC, Li G, Liaw PK, Liu RP (2016) The high-entropy alloys with high hardness and soft magnetic property prepared by mechanical alloying and high-pressure sintering. Intermetallics 70:82–87. https://doi.org/10.1016/j.intermet.2015.11.005

[30] Yavari AR, Desré PJ, Benameur T (1992) Mechanically driven alloying of immiscible elements. Phys Rev Lett 68:2235–2238. https://doi.org/10.1103/PhysRevLett.68.2235

[31] Suryanarayana C (2001) Mechanical alloying and milling. Prog Mater Sci 46:1–184. https://doi.org/10.1016/S0079-6425(99)00010-9

[32] Celis JP, Roos JR, Buelens C (1987) A mathematical model for the electrolytic codeposition of particles with a metallic matrix. J Electrochem Soc 134:1402–1408. https://doi.org/10.1149/1.2100680

[33] Yang B, Vehoff H (2007) Dependence of nanohardness upon indentation size and grain size—a local examination of the interaction between dislocations and grain boundaries. Acta Mater 55:849–856. https://doi.org/10.1016/j.actamat.2006.09.004

[34] Wang MG, Ngan AHW (2004) Indentation strain burst phenomenon induced by grain boundaries in niobium. J Mater Res 19:2478–2486. https://doi.org/10.1557/JMR.2004.0316

[35] Aifantis KE, Soer WA, De Hosson JTM, Willis JR (2006) Interfaces within strain gradient plasticity: theory and experiments. Acta Mater 54:5077–5085. https://doi.org/10.1016/j.actamat.2006.06.040

[36] Soer WA, De Hosson JTM (2005) Detection of grain-boundary resistance to slip transfer using nanoindentation. Mater Lett 59:3192–3195. https://doi.org/10.1016/j.matlet.2005.03.075

[37] Soer WA, Aifantis KE, de Hosson JTM (2005) Incipient plasticity during nanoindentation at grain boundaries in body-centered cubic metals. Acta Mater 53:4665–4676. https://doi.org/10.1016/j.actamat.2005.07.001

[38] Maier-Kiener V, Schuh B, George EP, Clemens H, Hohenwarter A (2017) Nanoindentation testing as a powerful screening tool for assessing phase stability of nanocrystalline high-entropy alloys. Mater Des 115:479–485. https://doi.org/10.1016/j.matdes.2016.11.055

[39] Zendejas Medina L, Tavares da Costa MV, Paschalidou EM, Lindwall G, Riekehr L, Korvela M, Fritze S, Kolozsvári S, Gamstedt EK, Nyholm L, Jansson U (2021) Enhancing corrosion resistance, hardness, and crack resistance in magnetron sputtered high entropy CoCrFeMnNi coatings by adding carbon. Mater Des. https://doi.org/10.1016/j.matdes.2021.109711

[40] Li X (2023) Electrodeposition of multi-component alloys: thermodynamics, kinetics and mechanism. Curr Opin Electrochem 39:101289. https://doi.org/10.1016/j.coelec.2023.101289

[41] Zangari G (2015) Electrodeposition of alloys and compounds in the era of microelectronics and energy conversion technology. Coatings 5(2):195–218. https://doi.org/10.3390/coatings5020195

[42] Girginov A, Tzvetkoff TZ, Bojinov M (1995) Electrodeposition of refractory metals (Ti, Zr, Nb, Ta) from molten salt electrolytes. J Appl Electrochem. https://doi.org/10.1007/BF00241947

[43] Zhao Y, VanderNoot TJ (1997) Electrodeposition of aluminium from nonaqueous organic electrolytic systems and

room temperature molten salts. Electrochim Acta 42(1):3–13. https://doi.org/10.1016/0013-4686(96)00080-1
[44] Abi-Akar H, Riley C, Maybee G (1996) Electrocodeposition of nickel−diamond and cobalt−chromium carbide in low gravity. Chem Mater 8:2601–2610. https://doi.org/10.1021/cm950483j
[45] Maurin G, Lavanant A (1995) Electrodeposition of nickel/silicon carbide composite coatings on a rotating disc electrode. J Appl Electrochem 25:1113–1121. https://doi.org/10.1007/BF00242538
[46] Sadeghi A, Sieber M, Hasannejad H, Scharf I, Lampke T (2016) Correlating the layer properties of Ni-alumina composite coatings and the mechanism of codeposition. Int J Chem 8:110. https://doi.org/10.5539/ijc.v8n2p110
[47] Narasimman P, Pushpavanam M, Periasamy VM (2011) Effect of surfactants on the electrodeposition of Ni-SiC composites. Port Electrochim Acta 30:1–14. https://doi.org/10.4152/pea.201201001
[48] Conway BE (2005) Modern Aspects of Electrochemistry. Kluwer Academic/Plenum Publishers, New York
[49] Chaudhari AK, Singh VB (2018) A review of fundamental aspects, characterization and applications of electrodeposited nanocrystalline iron group metals, Ni-Fe alloy and oxide ceramics reinforced nanocomposite coatings. J Alloys Compd 751:194–214. https://doi.org/10.1016/j.jallcom.2018.04.090
[50] Epelboin I, Wiart R (1971) Mechanism of the electrocrystallization of nickel and cobalt in acidic solution. J Electrochem Soc 118(10):1577. https://doi.org/10.1149/1.2407788
[51] Nakahara S, Felder EC (1982) Defect structure in nickel electrodeposits. J Electrochem Soc 129:45–49. https://doi.org/10.1149/1.2123789
[52] Ni L, Pocratsky RM, de Boer MP (2020) Origins of thin film delamination induced by electrodeposition and processing methods to overcome it. Thin Solid Films 697:137796. https://doi.org/10.1016/j.tsf.2020.137796
[53] Vazquez-Arenas J, Altamirano-Garcia L, Pritzker M, Luna-Sánchez R, Cabrera-Sierra R (2011) Experimental and modeling study of nickel electrodeposition including H^+ and water reduction and homogeneous reactions. J Electrochem Soc 158:D33. https://doi.org/10.1149/1.3515071
[54] Ritzert NL, Moffat TP (2016) Ultramicroelectrode studies of self-terminated nickel electrodeposition and nickel hydroxide formation upon water reduction. J Phys Chem C 120(48):27478–27489. https://doi.org/10.1021/acs.jpcc.6b10006
[55] Gomez E, Muller C, Proud WG, Valles E (1992) Electrodeposition of nickel on vitreous carbon: influence of potential on deposit morphology. J Appl Electrochem 22(9):872–876. https://doi.org/10.1007/BF01023732
[56] Cui CQ, Lee JY (1994) Effects of oxygen reduction on nickel deposition from unbuffered aqueous solutions: I deposition process and deposit structure. J Electrochem Soc 141(8):2030–2035. https://doi.org/10.1149/1.2055055
[57] U.I. Woltoamperometria (2015) Faculty of Chemistry, Warsaw University of Technology